UNIVERSITAT POLITÈCNICA DE CATALUNYA
BARCELONATECH
Escola Superior d'Enginyeries Industrial, Aeroespacial i Audiovisual de Terrassa

ESEIAAT
Bachelor's Thesis

Study of a descent system for atmospheric re-entry and landing of space vehicles

Report

Student: Muñoz Morales, Víctor
Director: Ortega, Enrique

Degree: Bachelor's degree in Aerospace Technology Engineering
Delivery Date: 27/04/2020

Universitat Politècnica de Catalunya
Escola Superior d'Enginyeries Industrial, Aeroespacial i Audiovisual de Terrassa

DECLARATION OF HONOR

I declare that,

- the work in this Degree Thesis is completely my own work,
- no part of this Degree Thesis is taken from other people's work without giving them credit,
- all references have been clearly cited.

I understand that an infringement of this declaration leaves me subject to the foreseen disciplinary actions by the *Universitat Politècnica de Catalunya - BarcelonaTECH.*

Student Name: Víctor Muñoz Morales
Signature:

Date: 27/04/2020

Title of the Thesis: Study of a descent system for atmospheric re-entry and landing of space vehicles

"Fix your course on a star and you'll navigate any storm"

Leonardo Da Vinci

Contents

Acknowledgements

First, I would like to express my sincere gratitude to all that people who have been close to help me throughout the work. To my classmates, teachers and friends that have been there following the progress of this project.

On the other hand, I would like to appreciate and thank my tutor, Enrique Ortega, for all the knowledge and effort he has made on this, for the help, consideration and support when things have become complicated. Also for accepting my proposal and agreeing to carry out this project that I wanted so much and for providing me with documentation that I have used throughout the project.

Finally, I want to acknowledge my family, my parents and brothers, who have always supported me even in the most difficult times. They have helped me become who I am now and make me believe that everything is possible if you give your best.

List of Figures

List of Tables

List of Symbols and Abbreviations

a	canopy height	m
A, B, C, P, Q, R, H	apparent mass constants	-
A_{ij}	influence coefficient	-
AR	Aspect Ratio	-
b	parafoil span	m
$b2c$	body to canopy axes transformation matrix	-
c	parafoil chord	m
C_D	parafoil drag force coefficient	-
C_{Di}	induced drag coefficient	-
C_{Dp}	parasite drag coefficient	-
C_{D_l}	parafoil lines drag coefficient	-
$C_{D_{PL}}$	payload drag coefficient	-
C_l,C_m,C_n	rolling, pitching and yawing moments coefficients	-
C_L	parafoil lift force coefficient	-
$C_{L_{PL}}$	payload lift coefficient	-
C_{L_α}	lift slope coefficient	-
C_Y	parafoil lateral force coefficient	-
d	suspension lines diameter	m
D, L, Y	aerodynamic forces	N
e	Euler's number	-
$\bar{F}$	force vector	N
g	gravity	m/s^2
GS	glide slope	rad or $^\circ$
$\bar{G}$	moment vector	N$\cdot m$
h	altitude	m
I_{ij}	moment of inertia ij-axes	$kg \cdot m^2$

$i2b$	inertial to body axes transformation matrix	-
$i2t$	inertial to track axes transformation matrix	-
K	PID parameter	-
K_p,K_i,K_d	proportional, integrative and derivative PID parameter	-
k_1, k_2	drag polar coefficients	-
L/D	aerodynamic efficiency	-
m	mass	kg
m_{add}	added mass	kg
Ma	Mach number	-
$m2c$	Matlab to canopy transformation frame matrix	-
num	number of suspension lines	-
N	number of horseshoe vortex elements	-
p, q, r	angular velocities in the body axes	rad/s
R	mean suspension line length	m
S	parafoil surface	m^2
S_r^B	cross-product matrix	-
t	thickness	m
t	time	s
TA	track angle	rad or °
TL	track length	m
u, v, w	linear velocities in the body axes	m/s
v^i	induced velocity	m/s
$\bar{V}$	velocity vector	m/s
V	velocity modulus	m/s
x, y, z	spatial coordinates in the inertial axes	m
$\dot{x}, \dot{y}, \dot{z}$	linear velocities in the inertial axes	m
$\bar{x}$	spatial coordinates vector	m
α	angle of attack	rad or °
α_{LO}	zero lift angle of attack	rad or °
β	side-slip angle	rad or °
γ	dihedral/anhedral angle	rad or °
γ	path angle	rad or °
Γ	rigging angle	rad or °
δ	aileron deflection	rad or °
Δt	time step	s

ε	canopy semi-aperture angle	rad or °
λ	taper ratio	-
Λ	sweep angle	rad or °
ρ	air density	kg/m^3
ϕ,θ,ψ	roll, pitch and yaw angles	rad or °
$\bar{\omega}$	angular velocity vector	rad/s

AGARD	Advisory Group for Aerospace Research and Development
AoA	Angle of Attack
AoS	Angle of Side-slip
CFD	Computational Fluid Dynamics
CG	Center of Gravity
CIMNE	International Center for Numerical Methods in Engineering
CIRA	Italian Aerospace Research Centre
DoF	Degrees of Freedom
DRAGONFLY	Deployable Ram-Air Glider with Optimum Navigation FLYing
ECTS	European Credit Transfer and Accumulation System
ESA	European Space Agency
ESEIAAT	Escola Superior d'Enginyeria Industrial Aeroespacial i Audiovisual de Terrassa
FEM	Finite Element Method
FLPP	Future Launchers Preparatory Programme
GNC	Guidance, Navigation and Control
GPS	Global Positioning System
GPSim	Gliding Parachute Simulator
HVLM	Horseshoe Vortex Lattice Method
ISA	International Standard Atmosphere
IXV	Intermediate eXperimental Vehicle
JPADS	Joint Precision Aerial Delivery System
LE	Leading Edge
LEO	Low Earth Orbit
LLT	Lifting Line Theory
MTRS	Mosquito Tactical Resupply System
NASA	National Aeronautics and Space Administration
PADS	Precision Aerial Delivery System
PDR	Preliminary Design Review
PEGASYS	Precision and Extended Glide Airdrop System
PRIDE	Programme for Reusable In-orbit Demonstrator in Europe
RIDER	Space Reusable Integrated Demonstrator for Europe Return
SR	Space Rider
SRR	System Requirements Review
TE	Trailing Edge

UK	United Kingdom
UPC	Universitat Politècnica de Cataluanya
USA	United States of America
VEGA	Vettore Europeo di Generazione Avanzata

Aim

The Space RIDER (Space Reusable Integrated Demonstrator for Europe Return) is an unmanned orbital spacecraft vehicle that will provide the European Space Agency (ESA) with a reusable integrated space transportation system for routine access and return from low earth orbit. The project is mainly led by the Italian PRIDE (Programme for Reusable In-orbit Demonstrator in Europe) program in collaboration with companies such as Thales Alenia and ESA. The inaugural flight is scheduled for 2022. The objective in the present work is to develope a 6 DoF flight simulator to analyze the atmospheric descent and landing of the Space Rider vehicle. The study will focus on the low subsonic descent stage. A maneuverable parafoil will be used for guiding autonomously the vehicle to the target touchdown point.

Scope

The scope of this study is detailed below:

- A 6 DoF dynamic model should be used for simulation of the Space RIDER maneuverable parafoil. The numerical code will be developed in Matlab®.
- The dynamic model will consider the Space RIDER gliding parachute and payload as a single rigid body to determine its trajectory and performance. The canopy will be already deployed, the flight will happen in nominal conditions and the relative movement between the canopy and the payload will be neglected. The effects of added mass will also be taken into account.
- The aerodynamic model will consider the parafoil as a small thickness canopy flying under nominal conditions (flow detachment effects are considered to be negligible). The canopy aerodynamics will be solved in the loop using a potential flow approach based on the Lifting Line Theory (Horseshoe Vortex Method). The number of horseshoe vortices in the discretization will be determined through a convergence study, in order to obtain satisfactory results without increasing the computational costs. The vehicle and parachute aerodynamic coefficients that cannot be obtained by an inviscid approach (e.g. drag) will be obtained from available experimental and numerical data.
- The parachute geometry should be defined in parametric form, considering the taper ratio, sweep and dihedral angle. Thickness is not considered in the aerodynamic method employed.
- A Proportional-Integral-Derivative (PID) subroutine will be used to allow the flight simulator perform autonomous navigation, guidance and control. The program may also be capable to modify the trajectory of the parafoil, acting on the control surfaces (trailing edge ailerons) along the descent.

- The simulator will be able to hold payloads from 2250 to 2550kg. The parafoil deployment will occur at an altitude between 10km and 6km at Mach number between 0.18 and 0.22. At touchdown the vertical speed must be below 3m/s, the horizontal speed below 35m/s and the landing accuracy within 50m from the target.

All the methodology, calculations and results obtained will be delivered in the Report, which will also include the program with the flight simulator used and the bibliographic references.

Requirements

In order to develop an accurate simulator for the parafoil, the following requirements are taken into account:

- Develop a 6 Degrees Of Freedom flight simulator for the ram-air maneuverable parafoil employed in the last stage of the re-entry and landing of the Space RIDER mission.
- Add a Proportional-Integral-Derivative (PID) control system capable to carry out autonomous flight and landing.
- Use the Lifting Line Theory in order to solve the aerodynamics in the loop.
- Consider the added mass in the dynamic model as the sum of the apparent mass and the mass included in the volume of the parachute.
- Payload requirements:
  - Weight from 2250 to 2550kg.
  - The characteristics of the Space Rider vehicle must be taken into account.
- Ram-air parachute deployment requirements:
  - Altitude between 10km and 6km.
  - Mach between 0.18 and 0.22.
- Touchdown requirements (at sea-level):
  - Vertical speed below 3m/s.
  - Horizontal speed below 35m/s.
  - Landing accuracy within 150m.
- The simulation methodology should have a low computational cost to allow real-time and parametric analyses.

Background

The Space RIDER is an unmanned orbital spacecraft vehicle that will provide the European Space Agency with a reusable integrated space transportation system for routine access and return from low earth orbit. The project is mainly led by the Italian PRIDE program in collaboration with companies such as Thales Alenia and ESA. The inaugural flight is scheduled for 2022. The construction and design of the atmospheric re-entry module is mainly in charge of the company Thales Alenia Space, but there are also other European aerospace companies and organizations that cooperate in the project. This is the case of the Spanish parachute manufacturer CIMSA Ingeniería en Sistemas, which is responsible for the development of the vehicle recovery system, and the International Center for Numerical Methods in Engineering (CIMNE) and the Escola Superior d'Enginyeria Industrial, Aeroespcial i Audiovisual de Terrassa (ESEIAAT), which collaborate providing numerical calculation supporting this task.

In order to determine the recovery trajectory and ensure the safety during the autonomous descent and landing of the parachute-payload system, rigorous testings and numerical simulations are required in advance through the use of flight and control computer program simulators. There are computer programs capable to solve the flight simulation proposed, using sophisticated numerical methods to obtain accurate results, for example fluid-structure interaction solvers are used in the context of the project to study the in-flight system dynamics. Nevertheless, such programs require several days to simulate only one parachute run, for example one second in the simulation could last several hours of CPU time, which makes it very difficult to perform practical trajectory and sensitivity analyses. This computational cost can be reduced considerably when it is only necessary approximated results of the descent trajectory.

In this work, the flight simulator will be based on an existing software called GPSim, intended for academic training. It was developed by David Pérez in his Final Degree Thesis,"Study of a methodology for the flight simulation of ram-air parachutes using a vortex-lattice aerodynamic

model", carried out in 2017 at the *Universitat Politècnica de Catalunya* (UPC). The GPSim flight simulator bases on a rigid-body 6 DoF dynamic model with the aerodynamics calculated in the loop. This is costlier than using parametric aerodynamics, but avoids the need of the system derivatives, which usually are not available in early stages of the projects and are difficult to estimate. The code is implemented in Matlab® and aims to provide fairly good results in relatively short time, which adapts well to the objective of the project.

Being Matlab® an internationally known and widely used program by many students and engineers, it is desired that the simulator can continue serving as an educational tool. On the other hand, according to the structure of the program, it could also be used to study other types of flying wings if modifying the parameters of the aircraft geometry and the simulation conditions. It is important to note that, due to the approximations that will be carried out (consideration of the canopy-vehicle as a single rigid body, negligible thickness of the canopy and the attached flow hypothesis), this methodology will be only accurate for problems in the range of the hypothesis stated in the scope of this project.

For the implementation of the program and the PID navigation system required, as mentioned before, the study will begin taking into account the results obtained by David Pérez in his Final Degree Thesis. The PID approach will be analyzed and improved, and a Lifting Line solver will be used to predict the parafoil aerodynamics. This methodology was first approached by Daniel Gutiérrez in his Final Degree Thesis, "Study and implementation of a control system for autonomous guided parachutes", presented in 2018 at the UPC. The idea here is to complete and validate this approach for application to a practical case of interest which is the Space RIDER system.

Chapter 1

Introduction

This chapter presents the literature review of the project. Firstly, it is exposed an overview of the historical background, development and applications of the parachute technology and aerial delivery systems, specifically for gliding parachutes. Then, the fundamental objectives and development of the ESA's Space Rider mission are presented. In the present work, the analysis focuses on the last stage of the re-entry of the aircraft, when the gliding parachute is deployed. Finally, several projects following similar objectives and methodologies, already carried out or currently in process, are shown. They will be used as references for the development of the present work.

1.1 Parachutes and Recovery Systems

The first documented references to the use of parachutes are dated from the 12th century in China, which were used to descend animals and people from high towers. Since then, the oldest documents and designs of parachutes found are in some sketches of Leonardo Da Vinci, in 1514. This prototype consisted of sealed linen cloth held open by a pyramid of wooden poles, about 7 meters long (Figure 1.1). In 1617, Fauste Veranzio built a rigid frame prototype following the Da Vinci's models, titled the *Homo Volans* (Flying Man), and jumped from a tower in Venice [1] [2].

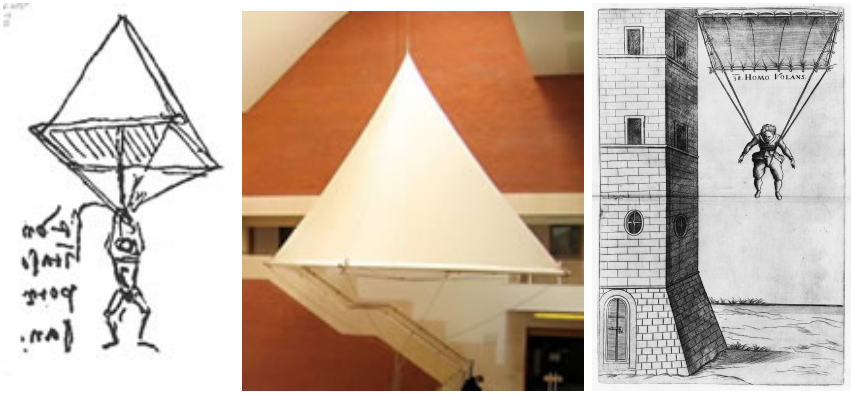

Figure 1.1: Leonardo Da Vinci's parachute (left and center) [3] and the *Homo Volans* [4]

Other rigid frame models were also built after these, for example those designed by the Montgolfier brothers, to descend animals from rooftops and balloons. However, it was not until October 22 of 1797 that André-Jaques Ganerin made the first successfully jump using a flexible parachute. It was done from a balloon in Paris and was the first demonstrable parachute descent in history [5]. From that moment and on, the use of parachutes for spectator entertainment purposes increased until the beginning of the 20th century. In one of the Ganerin jumps, a French astronomer realised that the parachute made oscillations during the descent and proposed to make a cut in the centre of the parachute, having success and thus introducing the also known as vent parachute. In 1808, it is dated the first emergency landing, when Jordaski Koparento descended safely from a burning balloon in Warsaw [1] [2].

It was not until the World War I that the use of the parachute became more practical than just entertainment. Both sides flew over to spy the enemy troops in hydrogen-filled balloons, which sometimes were hunted by the enemy and shot with machine-gun fires that could blow up the balloon. They had parachutes tied to the baskets in which the observers could jump and safe their lives in case of emergency, if they were lucky. There are dated more than 500 successful retrievals counting members of the British Balloon Wings and the United States Forces, regardless of the carried out by the German troops [1] [6].

When the first aircrafts appeared in the war, they didn't incorporate parachute recovery systems, due to the trouble of propelling it out of the cockpit. The life of the pilots was highly valued by the army, so a great study was carried out relating parachute materials and packing to solve this problem. The first recorded saving of life from an aircraft by using a parachute is dated in 1916, the parachute was just attached to the aircraft by static lines and it didn't

open since the pilot was outside of the cockpit. In 1919, Leslie L. Irvin made the first free parachute descent form 1000ft above the ground, standing some seconds in free falling and then deploying the parachute. After the end of the World War I, there was a revolution of new ideas for personnel and aircraft's rescue parachutes, which led to the development of new models as the Heinecke aircraft escape parachute in Germany (Figure 1.2) and the creation of new safety rules [1].

During the 20's, it was created the Hoffman triangle parachute, the first gliding parachute. In 1924, appeared the first military personnel parachute standardisation and the recovery system for private planes. Then in the 30's, the need for high aircraft decelerator for high speeds drove Georg Madelung to develop of the ribbon parachute (Figure 1.2). It provided low opening shock loads and a really good stability in pitch and introduced the slotted textile parachute. The worldwide tension due to the German rearmament and aircraft development boosted other governments to invest in parachutes and recovery systems, improving the aerodynamic and stability, materials and the inflation process.

Figure 1.2: Heinecke escape (left) [7] and Eurofighter Typhoon ribbon (right) [8] parachutes.

During the World War II, there were in many countries an over-riding need for reliability and improvement of this technology, specially in the United Kingdom, the United States and Germany. The Germans used parachutes to recover missiles and created the guided surface parachute. The USA was the first country that counted with airborne troops and aerial delivery of supplies and equipment, as well as the first to use nylon in the parachute's fabric. The UK progressed in high porosity shaped gore parachutes and the introduction of parachute clusters [9].

After the war, the USA army, promoted by the engagements in Vietnam, started a research of new parachute types and applications. In the early 60's, the need of controlling the parachute trajectory and delivering payloads to an specific target, motivated the development of new maneuverable or gliding parachutes, such as the ram-air inflated textile wing proposed by Domina Jalbert in 1961 (Figure 1.3). They were designed with higher glide ratios than the previous ones, which made possible its use in sports, as the skydiving.

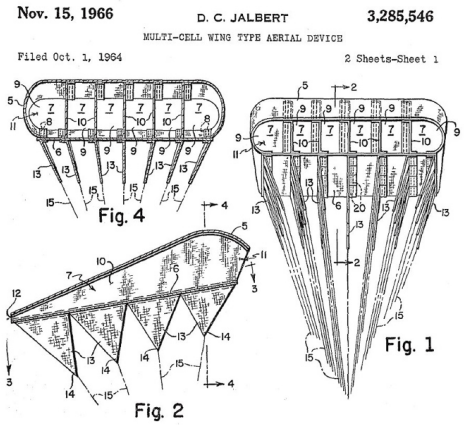

Figure 1.3: Domina Jalberg's ram-air parachute patent [10].

On the other hand, between the 60's and the 70's, the advance of aircraft and space missions technologies led to development of more exigent decelerators and the ribbon parachutes capabilities were improved. These parachutes, allowed space applications like re-entry vehicles recovery, allowing United States astronauts returning form the Moon in the Mercury, Gemini and Apollo missions, as well as those in the Soviet Union's Vostok and Soyuz space vehicles. In July 1976, the Viking spacecraft was capable to land in Mars for the first time using this kind of parachutes [1].

In the last four decades, the parachutes technology has performed a huge development, using new smart materials and improving their accuracy in the landing approach systems. With the evolution of computer science, there have also been created new numerical tools and simulators to predict their flight behaviour, thereby reducing designing and production costs and time. This development has allowed the increase of these kind of recovery systems in several studies and prototypes of the aerospace industry. Further, the important market that currently covers

paragliding and its popularity throughout the world must be highlighted.

Regarding the gliding parachute used in the last stage of re-entry of the Space Rider vehicle, it is one of the most recent parachute type and has been very developed in the previous 50 years. Despite this fact, its unique use on space missions was carried out by NASA with their X-38 Crew Return Vehicle program in 1999 and used successfully till 2002, being the largest parafoil used in history, with an area almost 1.5 times the wings of a Boeing 747 jumbo jet [11]. The European knowledge of the field has just remained confined to military cargo, entertainment and university studies [12].

Figure 1.4: X-38 Crew Return Vehicle [13].

1.1.1 Ram-air Parachute

The ram-air parachute, also called as parafoil, belongs to the family of maneuverable or gliding parachutes and is just one among all the different existing types of parachutes. Those are capable of generating a horizontal component of velocity of the parachute and its payload. Hence, it is possible for a system comprising a gliding parachute and payload to develop a resultant lift force. They consist on a flexible fabric wing with rectangular planform and a streamlined cross-section which is opened at the leading edge to allow air to enter and inflate the wing to a specified shape. They are more expensive than other gliding or conventional parachutes, but they offer higher gliding ratios and manoeuvrability, that allows them to be optimum for the development of precision aerial delivery systems. In order to provide and maintain a good

control, their Aspect Ratios are limited to a maximum of about $3-4$. The angle of descent γ_d is inversely proportional to the L/D ratio. High performance parafoils can reach L/D values between 4-5 or even higher [14].

Many universities are carrying out researches about this type of parachute and different companies have developed commercial models, which mainly aim to the defence market and skydiving industry. The USA government has developed a program called Joint Precision Airdrop Delivery System (JPADS) that combines the USA Army's Precision and Extended Glide Airdrop System (PEGASYS) with the USA Air Force's Precision Airdrop System (PAS) to meet joint requirements for precision airdrop. Some examples of companies that develop products that fulfil the precision airdrop requirements under the JPADS program are: Airborne Systems®, which has developed the DragonFly parafoil (Figure 1.5) and others that can deliver payload from 45 to 19500kg; and STARA Technologies Corp., which has developed the Mosquito Tactical Resupply System (MTRS) for medical supplies deliveries and payloads up to 70kg [6] [15].

On the other hand, the USA Navy Postgrade School and the University of Alabama in Huntsville employed in a research project the Snowflake system (Figure 1.5), from which references will be taken in this project. This small parafoil-payload system was the object of study of a precision airdrop system to evaluate advanced concepts of control for guided autonomous parafoils [16].

Figure 1.5: From left to right: Dragonfly [15], Mosquito, and Snowflake parafoils [16].

1.2 The Space Rider Project

The Space RIDER (Space Reusable Integrated Demonstrator for Europe Return) program aims to develop an affordable European space reusable transportation system. This will be launched by the Vega-C rocket and it is intended to perform experimentation and demonstration of multiple space application missions in Low Earth Orbit (LEO) [17].

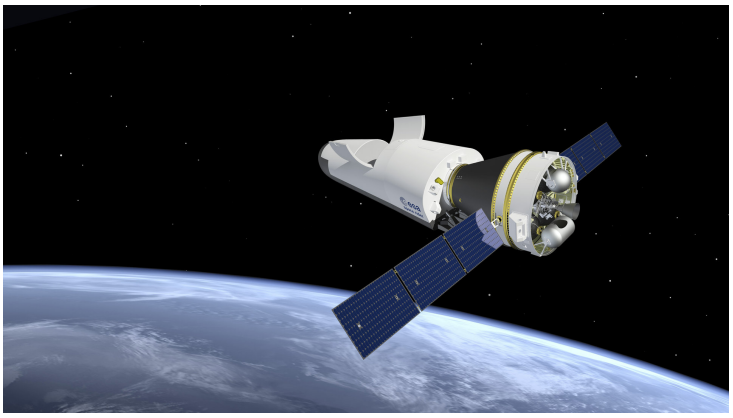

Figure 1.6: Space Rider vehicle in LEO [17].

The development of this project is led by the Italian PRIDE (Programme for Reusable In-orbit Demonstrator in Europe) program carried out by the Italian Aerospace Research Centre (CIRA), after the success of the IXV (Intermediate eXperimental Vehicle) experience launched on February of 2015. This proposal was submitted in the ESA's program called Future Launchers Preparatory Programme (FLPP) and approved in 2016 to be attempted as the new uncrewed orbital reusable spacecraft system of the European company, dating its first flight in 2022. After the success of the X-38 mission led by NASA during the years 1999 and 2002, ESA seeks to regain advantage with the use of gliding parachutes in re-entries in order to count with an affordable and routine access to space [12] [17].

Once accepted the mission development by ESA, Thales Alenia Space and Lockheed Martin were claimed to be the leading companies regarding the reentry and service modules designing and building, respectively. Both also count with more than 20 European companies of the space sector co-operating with the aim of the mission. This is the case of the Spanish parachute manufacturer CIMSA Ingeniería en Sistemas (see www.cimsa.com), which is responsible for the development of the vehicle recovery system, and the International Center for Numerical Meth-

ods in Engineering (CIMNE) and the Escola Superior d'Enginyeria Industrial, Aeroespcial i Audiovisual de Terrassa (ESEIAAT), which collaborate with CIMSA providing numerical calculation. Currently, the project has already passed the phase B1 (System Requirements Review, SRR) and B2 (Preliminary Design Review, PDR), and it remains in the phase C, which consists on the final design of the spacecraft, expected to be concluded in summer 2020.

Regarding the design of the Space Rider vehicle, the aeroshape selection studies based on multi-criteria decision analysis concluded that the best option was the Lifting Body "IXV 1:1", which had already demonstrated space entry and hypersonic/supersonic flight capabilities. It was also considered to add vertical fins to this shape for improving its control behaviour, the also called as "IXV 1:1 with Fins", but some CFD simulations finally concluded that the advantages do not compensate the increment in mass and vehicle complexity. However, this last model works as an alternative and will be studied and developed for following Space Rider missions. Both models are shown in Figure 1.7 [18].

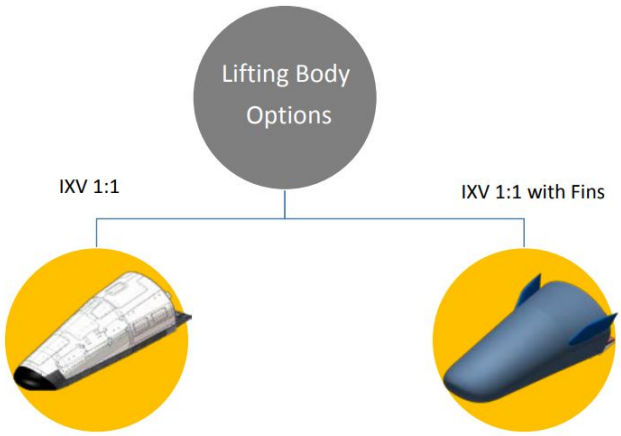

Figure 1.7: IXV 1:1 and IXV 1:1 with Fins [18].

ESA made an announcement in 2018 for giving the opportunity to fly small payloads onboard first flight in 2022. It will be launched on Vega-C from Europe's Spaceport in Kourou, French Guiana, remain in space in a low-drag altitude orbit for about two months. This expected two-month long maiden flight and mission will send and return to Earth the payload on the vehicles cargo bay and it will be followed by several missions in order to verify its wide range of capabilities in different orbits. The vehicle will operate at different orbital inclinations and heights, from equatorial to high-latitude, with a payload mass capability up to 800kg.

Its landing is planned in the Azores archipelago, which is a suitable European landing location for missions that require high-latitude inclinations. This target position allows the aircraft to return at the same latitude as its operational orbit, requiring fewer deorbiting manoeuvres, which will simplify notably the descent process form orbit to Earth [19].

The main concept operations of the Space RIDER mission are shown in Figure 1.8:

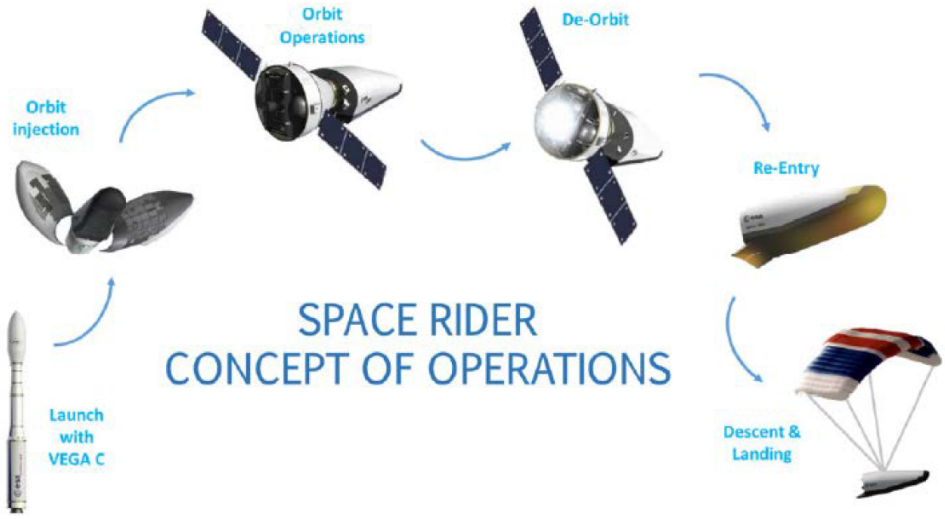

Figure 1.8: Concept operations of the Space RIDER [18].

For the future work of the Space Rider project, it is planned to increase the volume of the multipurpose cargo bay, which will allow to admit more and larger payloads on each mission. In 2025, ESA aims to privatize the Space RIDER, with Arianespace, the probable operator. Until the date, it will serve for investigations and demonstration of its proper functioning in different applications.

1.2.1 Space Rider Re-entry, Descent and Landing

Since the early phases of the project, in order to allow preliminary analysis of the descent and landing of the system, some high-level requirements were established and applied along the design and development stages. The most relevant for the purpose of this work are the following:

- Touchdown accuracy on open-field: $150m$
- Vehicle maximum weight: $2550kg$
- Limit landing speeds: horizontal $35m/s$; vertical $3m/s$

The descent system architecture selection was based on other vehicles that required a controlled descent with a parafoil, such as the X-38, the JPADS or the PAS, and it considered the minimization of the development cost and time, the risk of failures, and the mass and volume of the subsystems. It is divided in two different main phases: the passive one, that slows down the vehicle after the re-entry and deployment of a circular drogue parachute decelerator; and the controlled one, that guides the vehicle and makes it land closer to the defined landing target by using a gliding parachute. This descent phase strategy is shown in Figure 1.9 [20]:

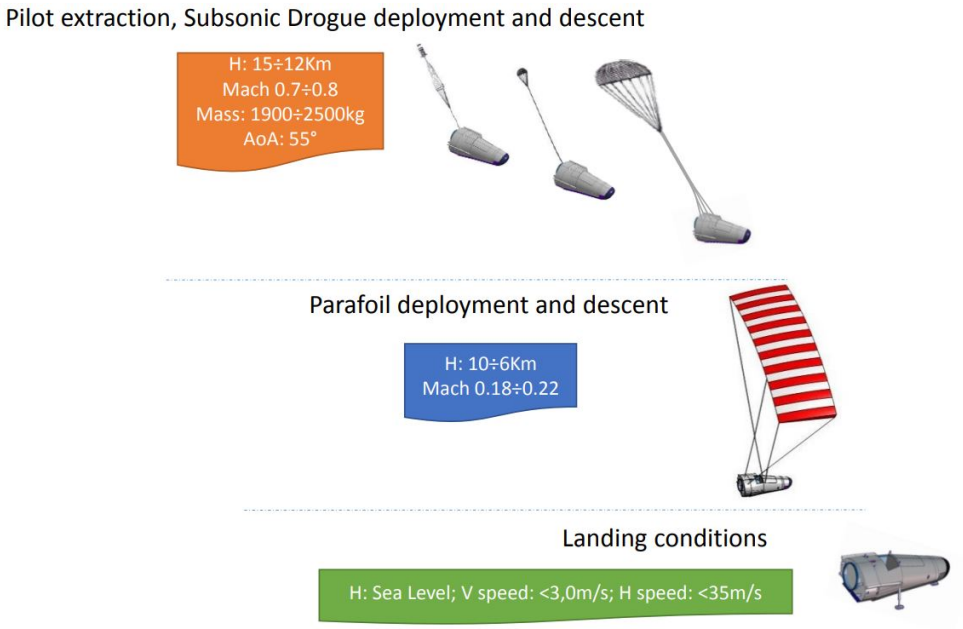

Figure 1.9: Space Rider descent phase strategy [20].

This work is focused on the last stage, which aims to land as close as possible to the desired target point. For this purpose, the self-directed parafoil is deployed at an altitude between 6-10km. This parafoil is based on the model reported in [21], which used Space Rider values offered by Thales Alenia. Some geometric specifications are detailed in Table 1.1:

$S[m^2]$	100
$b[m]$	17.32
$c[m]$	5.77
$AR[-]$	3
$t/c[-]$	0.18

Table 1.1: Space Rider parafoil dimensions.

Once the ram-air parachute is deployed, a Guidance Navigation and Control (GNC) system steers the parachute by pulling the lines connected to the brakes of the parafoil with the winches installed on the spacecraft. This system will guide the vehicle to the landing point and will reduce the vertical landing speed with the "flare" manoeuvre.

Basically, this final stage is divided in the typical phases of an automatic approach system [20]:

1) Homing phase: The GNC system steers the vehicle towards the landing target point.

2) Loiter: The system will remain near the target while it reduces its altitude.

3) Approach: When the vehicle is under a certain altitude, the GNC guides the system performing the correct manoeuvres to land near the target point and with the right velocity.

4) Landing: The vehicle extracts the landing gear and lands.

1.3 Approaches for Parachute Trajectory Simulation

There are abundant literature on the simulation of the descent of gliding parachutes using different methods for the aerodynamic study. The flight simulator in this work is developed on the basis of an existing software called GPSim, which was developed by D. Pérez in his Final Degree Thesis [6], carried out in 2017 at the *Universitat Politècnica de Catalunya* (UPC). In this work, the 6 DoF simulator was satisfactorily implemented, but the aerodynamic model used (a Vortex Lattice Method) showed uneffective due to the high computational cost. After this thesis, it was concluded that the GPSim flight simulator should be improved for performing such studies (for example using cheaper simulation approaches). Efficiency can be also increased by using more specific programming languages, but Matlab® allows to obtain satisfactory results in relatively short development time, which adapts well to the academic objective of the project.

Previous works have already tried to reduce the computational cost of GPSim by implementation of an aerodynamic solver based on the the Lifting Line Theory. This was developed by D. Gutiérrez in his Final Degree Thesis [22], presented in 2018 at the UPC.

In the context of the Space Rider project, N. Glouchtchenko, an ex-student of the *Politecnico de Milano*, worked in colaboration with Thales Alenia during his Master Thesis [21], presented in July of 2018. The author studied the Space Rider gliding parachute developing a 12 DoF flight simulator, considering the parafoil and the payload as separate bodies. This work was mainly focused on studying the inflating process and the developing of the PID control system. The major part of the aerodynamics was taken from the article published by J.S. Lingard in 1995 [23].

Regarding the effects of the apparent mass on the dynamics of the parafoil, there are several studies for approximation in different cases and parafoil geometries. One of the best references for this concept consideration are the results detailed by P. Lissaman and G. Brown in their work [24], in 1993. G. Kowaleczko also published some results of the apparent mass and inertia moments related with the considerations of Lissaman and Brown in [25].

Other works within this field that will serve as a reference in the present work are the ones carried out by O.A. Yakimenko et al. in his book [26]. Also, the simulations and parafoil control studies made by B.E. Tweddle in [27] and by N. Slegers and M. Costello in [28]. Furthermore, the control system will follow the bases and relevant data will be obtained from the 6 DoF simulator developed by CIMNE in [16].

Chapter 2

Dynamic Model

The study of the flight mechanics of the parafoil during the descent flight will allow to estimate its performances, trajectory and stability. This chapter develops the dynamic equations of the system, considering the most appropriate axes. In this sense, it is supposed the system (gliding parachute + Space Rider vehicle) as a rigid solid with a fixed Center of Gravity (CG). This consideration makes it easier to calculate the trajectory and spin of the system. By a time integrator, it will be obtained the trajectory and linear and angular velocities of the parafoil at each time step analysed. Then, the PID system will control the position of the control surfaces of the parafoil in order to guide it to the desired landing point. The parafoil counts with one control surface located at the canopy trailing edge, controlled by the lines attached to the vehicle. This could be considered as an aileron and, as it will be seen in the control section, it will be capable to change the dynamics of the parafoil along the flight. For the validation of the dynamic and aerodynamic solvers, it will be studied also the small parafoil-payload system called Snowflake. Since there are several references that have used this model [6] [16] [22], it makes it easier to verify the correct performance of the simulator.

2.1 Axes Definition

In order to estimate the desired parameters of the descent, there will be considered 6 different reference axes. Some are used in the aerodynamic and control codes, but they are introduced in this section to detail their relationship with the axes used in the dynamic solver [29] .

- **Inertial Axes ($F_i(0_i, X_i, Y_i, Z_i)$):**
  Rotating topocentric system in which X and Y rotate in solidarity with the Earth in a tangential plane. O_i is a point of the Earth surface, X_i points North, Y_i points East and Z_i points the Earth center. They are the most appropriate reference axes to determine the trajectory of the parachute once introduced the initial position and the landing target.

- **Body Axes ($F_b(0_b, X_b, Y_b, Z_b)$):**
  Attached to the canopy symmetry plane. O_b is located in the CG, X_b in the symmetry plane pointing forward, Y_b pointing to the left side of the parachute due to the right handed law and Z_b in the symmetry plane pointing down and perpendicular to the other axes. These axes determine the performances of the parafoil.

- **Wind Axes ($F_w(0_w, X_w, Y_w, Z_w)$):**
  Attached to the relative wind seen by the canopy ($V_{cg} - V_{wind}$). O_w is located in the CG, X_w points the aerodynamic velocity $\bar{V}$, Y_w follows again the right handed law and Z_w in the symmetry plane pointing down and perpendicular to the other axes.

- **Canopy Axes ($F_c(0_c, X_c, Y_c, Z_c)$):**
  Attached to the canopy, showing an inclined angle with respect to the body axes due to the rigging angle of the canopy. O_w is located in the aerodynamic centre of the canopy, X_w in the symmetry plane pointing forward, Y_w follows the right handed law and Z_w in the symmetry plane pointing down and perpendicular to the other axes.

- **Matlab Axes ($F_m(0_m, X_m, Y_m, Z_m)$):**
  Used to make it easier the discretization of the horseshoe vortices along the span for the aerodynamics solver. O_m is located in the aerodynamic centre of the canopy, X_m is located in the symmetry plane pointing backward, Y_m follows the right handed law and Z_m points upward in the symmetry plane and perpendicular to X_m and Y_m.

- **Track Axes ($F_t(0_t, X_t, Y_t, Z_t)$):**
  Considered only for control functions. O_t is located on the target point and the axes orientation depend on the parachute position, as can be seen in Eq. 2.7.

In Figure 2.1, it is shown a basic sketch of the directions of the inertial, body, canopy and Matlab reference axes:

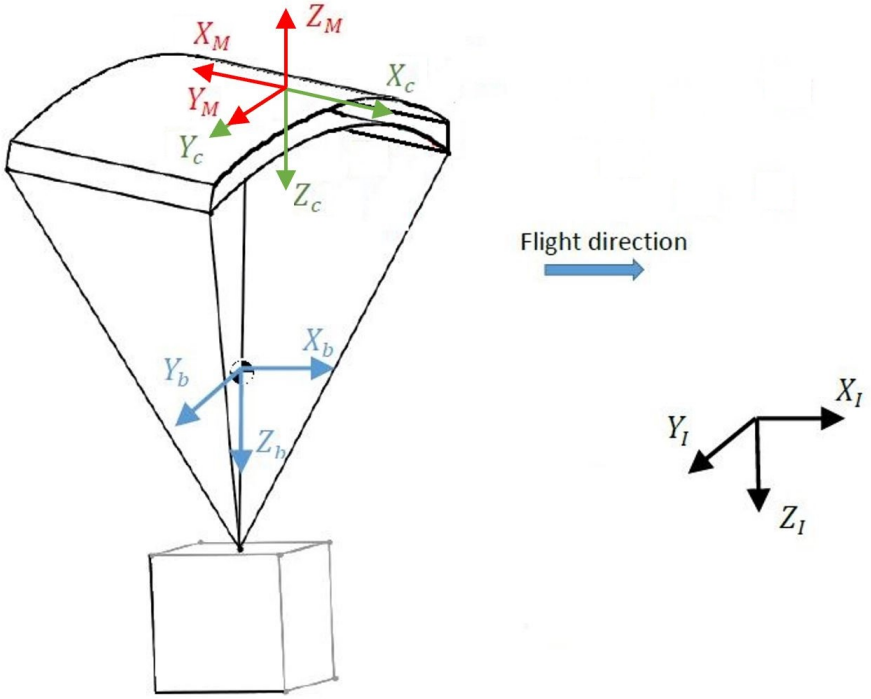

Figure 2.1: Inertial, body, canopy and Matlab reference axes [6].

In order to determine the dynamics of the parachute during the code loop execution, it will be required transformations from one frame to another. For this reason, there will be used the Euler angles (δ_1, δ_2 and δ_3) and transformation matrices [29].

- Rotation matrix from inertial axes to body axes:

$$i2b = \begin{bmatrix} c(\theta)c(\psi) & c(\theta)s(\psi) & -s(\theta) \\ s(\phi)s(\theta)c(\psi) - c(\theta)s(\psi) & s(\phi)s(\theta)s(\psi) + c(\theta)c(\psi) & s(\phi)c(\theta) \\ c(\phi)s(\theta)c(\psi) + s(\theta)s(\psi) & c(\phi)s(\theta)s(\psi) - s(\theta)c(\psi) & c(\phi)c(\theta) \end{bmatrix} \tag{2.1}$$

being ψ (δ_1) the yaw angle, θ (δ_2) the pitch angle and ϕ (δ_3) the roll angle. These Euler angles and transformations are shown in Figure 2.2. To reduce the size of the matrices in the document, the sines, cosines and tangents are represented as s, c and t, respectively.

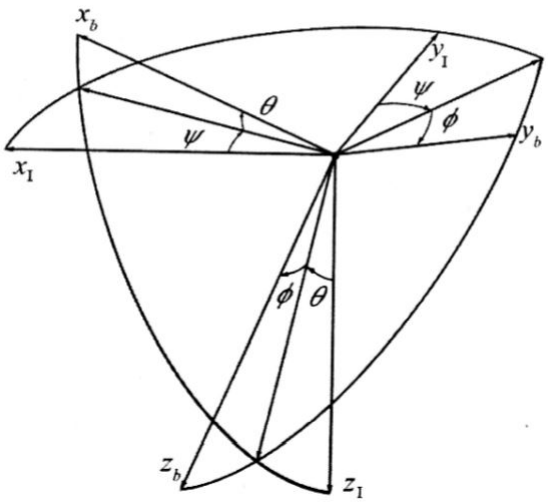

Figure 2.2: Euler angles for inertial to body axes transformation [29].

- Rotation matrix from inertial axes to wind axes:

$$i2w = \begin{bmatrix} c(\gamma)c(\chi) & c(\gamma)s(\chi) & -s(\gamma) \\ s(\mu)s(\gamma)c(\chi) - c(\gamma)s(\chi) & s(\mu)s(\gamma)s(\chi) + c(\gamma)c(\chi) & s(\mu)c(\gamma) \\ c(\mu)s(\gamma)c(\chi) + s(\gamma)s(\chi) & c(\mu)s(\gamma)s(\chi) - s(\gamma)c(\chi) & c(\mu)c(\gamma) \end{bmatrix} \tag{2.2}$$

  where χ (δ_1) is the yaw angle, γ (δ_2) the pitch angle and μ (δ_3) the roll angle. The Euler angles and transformations follow the same methodology as shown in Figure 2.2.

- Rotation matrix from wind axes to body axes:

$$w2b = \begin{bmatrix} c(\alpha)c(\beta) & -c(\alpha)s(\beta) & -s(\alpha) \\ s(\beta) & c(\beta) & 0 \\ s(\alpha)c(\beta) & -s(\alpha)s(\beta) & c(\alpha) \end{bmatrix} \tag{2.3}$$

  being $-\beta$ (δ_1) the Side-slip Angle and α (δ_2) the Angle of Attack (AoA).

- Rotation matrix from body axes to canopy axes:

$$b2c = \begin{bmatrix} c(\Gamma) & 0 & -s(\Gamma) \\ 0 & 1 & 0 \\ s(\Gamma) & 0 & c(\Gamma) \end{bmatrix} \tag{2.4}$$

  where Γ is the rigging angle of the canopy, as it is shown in Figure 2.3.

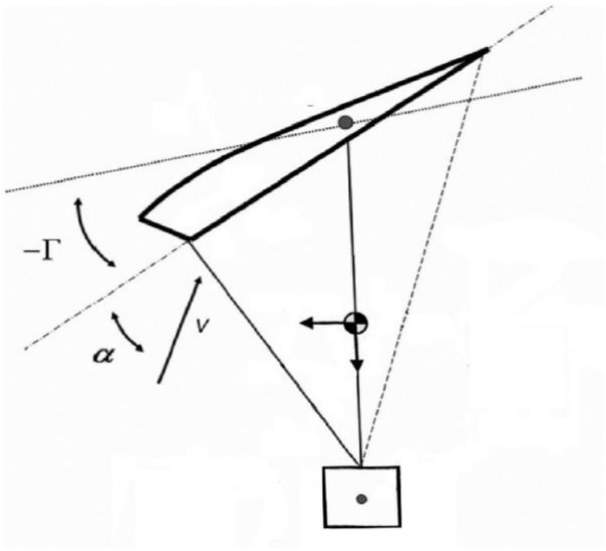

Figure 2.3: Rigging angle [16].

- Rotation matrix from Matlab axes to canopy axes:

$$m2c = \begin{bmatrix} -1 & 0 & 0 \\ 0 & 1 & 0 \\ 0 & 0 & -1 \end{bmatrix} \tag{2.5}$$

- Rotation matrix from inertial axes to track axes:

$$i2t = \begin{bmatrix} -s\left(TA - \frac{\pi}{2}\right) & c\left(TA - \frac{\pi}{2}\right) & 0 \\ c\left(TA - \frac{\pi}{2}\right) & s\left(TA - \frac{\pi}{2}\right) & 0 \\ 0 & 0 & -1 \end{bmatrix} \tag{2.6}$$

  being TA the track angle. It can be calculated as:

$$TA = cos^{-1}\left(\frac{PTN}{TL}\right) \tag{2.7}$$

  where PTN is the initial north position of the target and TL the track length from the parachute deployment point to the target point.

Notice that all the transformation matrices shown are orthogonal and thus, the inverse matrices can be obtained with the transpose. This fact will constantly be used during the code execution, changing from one frame to another.

2.2 Input Data

This section details the simulation input data. This include geometry specifications of the parafoil, masses and inertias, and the conditions for the descent. Values will be given for the Snowflake and Space Rider parachutes simulated in this work.

2.2.1 Geometry Specifications

The geometry specifications are given according to the parameters shown in Figure 2.4:

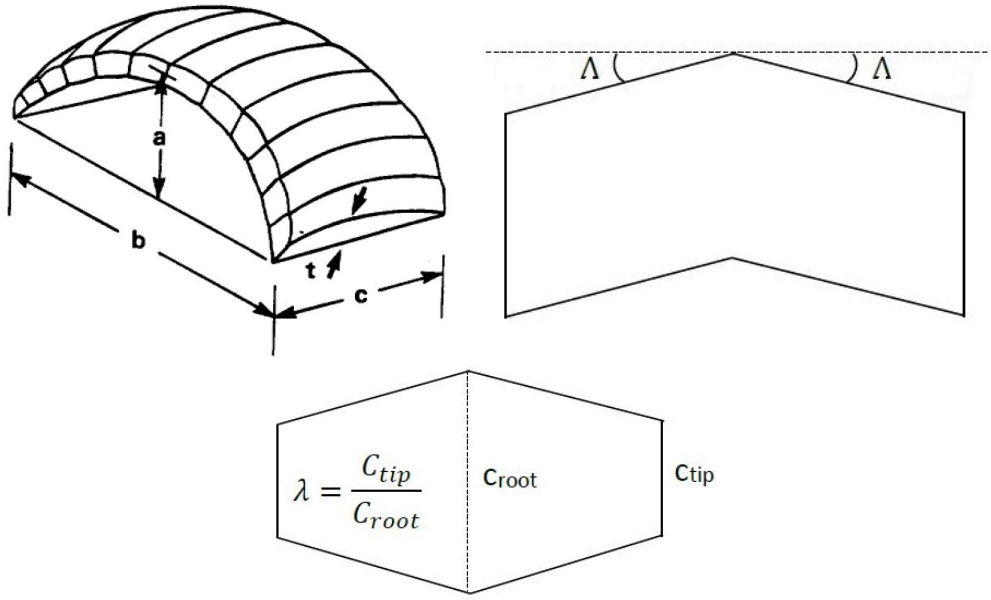

Figure 2.4: Parafoil geometry parameters [6] [21].

where b is the span, c the chord, a the maximum height, t the thickness, Λ the sweep angle of the leading edge (LE) and λ the taper ratio. Also, R is the length of the external lines of the canopy and ε_0 is the semi-aperture angle of the canopy.

	S $[m^2]$	**b [m]**	**c [m]**	**a [m]**	**AR [-]**	$\varepsilon_0[^o]$	**R [m]**	**t/c [-]**
Snowflake	0.93	1.36	0.69	0.1	2.45	22.5	1.78	0.18
Space Rider	100	17.32	5.77	1.27	3	56.44	10.39	0.18

Table 2.1: Geometry specifications of the parachutes used in this work.

Due to structural conditions, this type of parachute does not have high sweep angles. As there are no references detailing these angle for the Space Rider parafoil prototype, it is decided to adopt $\Lambda = 5^o$ which is a relatively small value and gives good longitudinal stability of the system. Regarding the taper ratio, it is considered that the root and tip chords are equal and thus $\lambda = 1$.

On the other hand, parafoils also count with two control surfaces in their trailing edge that operate as ailerons. The mechanism of these consists of curving the fabric from the trailing edge by stretching the suspension lines, thus deforming the chord line in some sections of the parafoil, as shown in Figure 2.5. Although their position cannot be clearly defined, based on the position of the brake lines, it is considered that they start at a distance of 70% of each semi-span from the root and end at the tips.

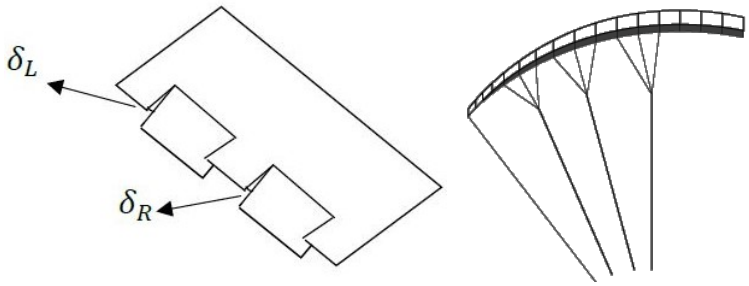

Figure 2.5: Control surfaces geometry [6] [30].

It is also worth mentioning the coordinates with respect to the CG of the points where the different forces of the system are applied. This process is called the trimming of the system and each model has its configuration, depending on the geometry and characteristics of the flight to be made, along with the stability requirements of the system. This includes the position of the payload ($\bar{x}_{PL}$), the aerodynamic center of the canopy ($\bar{x}_A$) and the apparent mass center ($\bar{x}_{AM}$).

In the following chapter, it will be explained that according to the HVM, the aerodynamic center is located at a distance of $c/4$ from the leading edge (wing sweep is small). The parafoil can operate with a rigging angle, modifiable or not during descent, which can change the position of the aerodynamic center with respect to the CG. On the other hand, according to the rigid solid condition, the vehicle will always be located on the z-body axis below the CG. Regarding the position of the CG of the system, considering that the payload weight is much larger than that of the parafoil, it is considered to be located in the same position as the vehicle.

2.2.2 Mass and Inertia

The mass and the moments of inertia of the system will remain constant throughout the descent. These values are obtained from experimental data. For the case of the Space Rider, the payload mass has been taken from the requirements established by the space mission, adopting the maximum stipulated value. The inertias have been taken from the model studied in [21]. On the other hand, both the mass and inertias of the Snowflake system have been taken from [16].

	Snowflake	**Space Rider**
Mass [kg]	2.37	2550
$I_{xx}[kg \cdot m^2]$	0.423	12011
$I_{yy}[kg \cdot m^2]$	0.401	4420
$I_{zz}[kg \cdot m^2]$	0.053	16232
$I_{xz}[kg \cdot m^2]$	0.030	3812

Table 2.2: Masses and inertias of the Snowflake and Space Rider systems.

In addition to the mass of the system, it must also be taken into account the air mass trapped into the volume of the canopy and that accompanies the system during the descent. As stated in [21], this air mass can be estimated by means of Eq. 2.8:

.

$$m_{add} = \rho t c \varepsilon_0 (2R + (1 - 2\zeta)\xi) \tag{2.8}$$

where ζ is a normalized value related with the geometry of the parafoil, usually equal to 0.25, and ξ is given by the following expression:

$$\xi = \frac{c}{1 + \Gamma^2} \tag{2.9}$$

As can be seen, this added mass depends on the air density, a value that varies throughout the descent. Therefore, this equation must be included in the loop of the program. In the same way, ξ depends on rigging angle, a value that will be modifiable according to the instructions given by the GNC control system. At sea level, this mass will represent for the Snowflake and Space Rider systems an added mass of $0.081kg$ and $171.169kg$, respectively. Thus, it is not a relevant effect for the Snowflake system, while for the Space Rider it is quite considerable.

2.2.3 Simulation Conditions

The GPSim simulator requires definition of several conditions throughout the descent: air density, wing direction, gravity, etc. These values must be considered in every step of the time integrator loop, in order to give the most accurate to reality values throughout the descent. The ram-air parafoil will be deployed at a height range between 6 and $10km$ with respect to the ground, which means that the descent will only take place in the troposphere. The study should be focused on the conditions of this lower layer of the atmosphere.

According to the ISA atmosphere, the air density decreases with the increment of height. The following expression allows to estimate the density value on every time step of the loop [31]:

$$\rho = \rho_0 \cdot \left(1 - 22.557 \cdot 10^{-6} \cdot h\right)^{4.256} \tag{2.10}$$

where $\rho_0 = 1.225 kg/m^3$ is the constant value of the air density at sea level and h is the height of the parafoil with respect to the ground. With the density, it is possible to estimate by the ISA equations the values of pressure for each point of the descent.

For the wing velocity, in the simulations will be considered neglected or parallel to the Earth surface, it means in the inertial XY-plane assuming the flat Earth hypothesis. The wing velocity will be given in the Inertial Axes and transformed into Body Axes to obtain the reference velocity of the centre of gravity of the system.

The gravity could be considered constant along the descent because the deployment altitude is not high enough to make gravity change considerably. Despite this fact, in order to obtain a better result for high payload masses, it will be considered the following expression that determines the small variations of the gravity factor:

$$g = g_0 \left(1 - \frac{2h}{R} + \frac{3h^2}{R^2}\right) \tag{2.11}$$

where $g_0 = 9.80665 m/s^2$ is the constant value of the gravity at sea level and $R = 6371 km$ is the Earth radius.

Regarding the input positions of the parafoil, it will always start its descent looking towards the North direction of the system, at the origin of coordinates of the inertial axis. The position of the landing point is defined into the program according to convenience, within the achievable range of flight of the system.

2.3 Dynamic Equations

The trajectory and velocities of the parachute can be obtained by using Newton's second law. As mentioned before, the entire system (parafoil + vehicle) is considered as a single rigid solid and its mass will be constant, as there's no mass missing during the flight. The equations are developed below [29]:

$$\sum \bar{F} = \frac{d}{dt}(m\bar{V}) = m\frac{dV}{dt} \tag{2.12}$$

where $\bar{F}$ are the external forces and $\bar{V}$ the absolute velocity in the inertial axes. In order to solve Eqs. 2.12, it is desired to pass it to body axes:.

$$\sum \bar{F}\Big|_b = m\left[\dot{\bar{V}}_b + \bar{\omega}_b \times \bar{V}_b\right] \tag{2.13}$$

where $\dot{\bar{V}}_b$ are the accelerations of the system and $\bar{\omega}_b \times \bar{V}_b$ the spin of the reference system.

$$\begin{pmatrix} F_x \\ F_y \\ F_z \end{pmatrix} = m\left[\begin{pmatrix} \dot{u} \\ \dot{v} \\ \dot{w} \end{pmatrix} + S_w^B \begin{pmatrix} u \\ v \\ w \end{pmatrix}\right] = m\begin{pmatrix} \dot{u} - rv + qw \\ \dot{v} + ru - pw \\ \dot{w} - qv + pv \end{pmatrix} \tag{2.14}$$

being S_w^B the cross-product matrix of the angular velocity expressed in the Body Axes:

$$S_w^B = \begin{bmatrix} 0 & -r & q \\ r & 0 & -p \\ -q & p & 0 \end{bmatrix} \tag{2.15}$$

Then, developing the kinetic moment theorem, it is possible to determine the moments:

$$\sum \bar{G} = \frac{d\bar{h}}{dt} \tag{2.16}$$

where $\bar{G}$ are the moments with respect to the CG and $\bar{h}$ is the inertial moment and it is determined as follows:

$$\bar{h} = \bar{\bar{I}}\bar{\omega} = \begin{bmatrix} I_x & -J_{xy} & -J_{xz} \\ -J_{yx} & I_y & -J_{yz} \\ -J_{zx} & -J_{zy} & I_z \end{bmatrix} \begin{pmatrix} p \\ q \\ r \end{pmatrix} = \begin{pmatrix} I_x p - J_{xz} r \\ I_y q \\ -J_{xz} p + I_z r \end{pmatrix} \tag{2.17}$$

where $\bar{\bar{I}}$ is the inertial tensor and $\bar{\omega}$ is the absolute angular speed of the system.

Finally, there are obtained the following equations for the moments in the Body Axes:

$$\sum \bar{G}\Big|_b = \frac{\partial \bar{h}}{\partial t}\Big|_b + \bar{\omega}_b \times \bar{h}_b \tag{2.18}$$

$$\begin{pmatrix} L \\ M \\ N \end{pmatrix} = \begin{pmatrix} I_x\dot{p} - J_{xz}\dot{r} \\ I_y\dot{q} \\ I_z\dot{r} - J_{xz}\dot{p} \end{pmatrix} + S_w^B \begin{pmatrix} I_x p - J_{xz} r \\ I_y q \\ I_z r - J_{xz} p \end{pmatrix} = \begin{pmatrix} I_x\dot{p} - J_{xz}(\dot{r} + pq) + qr(I_z - I_y) \\ I_y\dot{q} + J_{xz}(p^2 - r^2) - pr(I_z - I_x) \\ I_z\dot{r} + J_{xz}(qr - \dot{p}) + pq(I_y - I_x) \end{pmatrix} \tag{2.19}$$

In order to determine the linear and angular velocities, the system equations will be integrated in time. Figure 2.6 schematizes all these main forces, moments and velocities in the Body Axes:

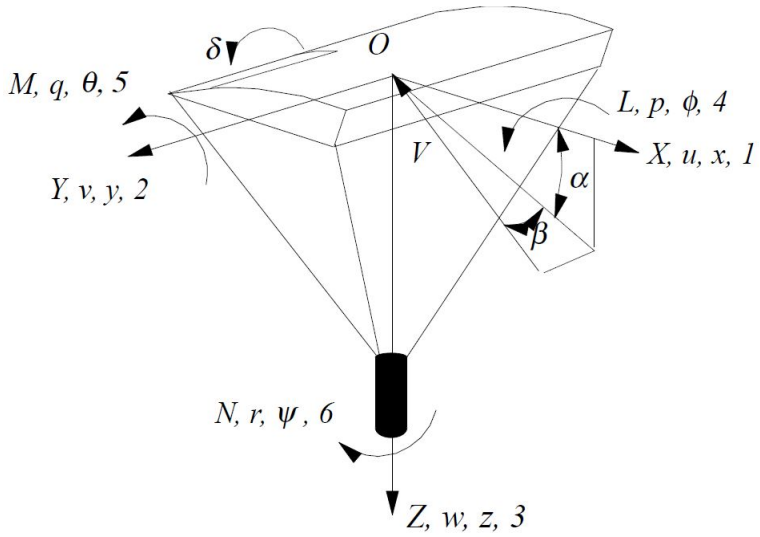

Figure 2.6: Dynamic parameters [23].

The total external forces and moments consist on the aerodynamic loads of the canopy and the payload, the weight of the system and the effects of the added mass (included + apparent):

$$\sum \bar{F} = \bar{F}_A + \bar{F}_{AM} + \bar{F}_G + \bar{F}_{PL} \tag{2.20}$$

$$\sum \bar{G} = \bar{G}_A + S^B_{CG.A} \times \bar{F}_A + \bar{G}_{AM} + S^B_{CG.AM} \times \bar{F}_{AM} + S^B_{CG.G} \times \bar{F}_G + S^B_{CG.PL} \times \bar{F}_{PL} \tag{2.21}$$

being $S^B_{CG.A}$, $S^B_{CG.AM}$, $S^B_{CG.G}$ and $S^B_{CG.PL}$ the cross-product matrix of the vectors from the CG to the aerodynamic centre of the canopy, the apparent mass centre, the CG and the aerodynamic

centre of the payload in the body axes, respectively. These cross-product matrix deal with the following convention for two vectors $r = (r_x \quad r_y \quad r_z)$ and $F = (F_x \quad F_y \quad F_z)$:

$$S_r^B \times \bar{F} = \begin{bmatrix} 0 & -r_z & r_y \\ r_z & 0 & -r_x \\ -r_y & r_x & 0 \end{bmatrix} \begin{pmatrix} F_x \\ F_y \\ F_z \end{pmatrix} \tag{2.22}$$

The forces and moments related with the aerodynamics of the parafoil will be determined in the aerodynamics section. The forces and moments related to the added mass are are discussed in the following section. Regarding the gravitational forces or weight of the system, it will be calculated in body axes as:

$$\bar{F}\big|_b = i2b \begin{pmatrix} 0 \\ 0 \\ mg \end{pmatrix} = mg \begin{pmatrix} -s(\theta) \\ c(\theta)s(\phi) \\ c(\theta)(c\phi) \end{pmatrix} \tag{2.23}$$

To estimate the trajectory, it is needed to define the kinematic of the system. The velocities will be computed in the body zxes, but they must be expressed in the inertial axes:

$$\begin{pmatrix} \dot{x} \\ \dot{y} \\ \dot{z} \end{pmatrix} = i2b^T \begin{pmatrix} u \\ v \\ w \end{pmatrix} = \begin{bmatrix} c(\theta)c(\psi) & s(\phi)s(\theta)c(\psi) - c(\phi)s(\psi) & c(\phi)s(\theta)c(\psi) + s(\phi)s(\psi) \\ c(\theta)s(\psi) & s(\phi)s(\theta)s(\psi) + c(\phi)c(\psi) & c(\phi)s(\theta)s(\psi) - s(\phi)c(\psi) \\ -s(\theta) & s(\phi)c(\theta) & c(\phi)c(\theta) \end{bmatrix} \begin{pmatrix} u \\ v \\ w \end{pmatrix} \tag{2.24}$$

$$\begin{pmatrix} \dot{\phi} \\ \dot{\theta} \\ \dot{\psi} \end{pmatrix} = \begin{bmatrix} 1 & s(\phi)t(\theta) & c(\phi)t(\theta) \\ 0 & c(\phi) & -s(\phi) \\ 0 & s(\phi)/c(\theta) & c(\phi)c(\theta) \end{bmatrix} \begin{pmatrix} p \\ q \\ r \end{pmatrix} \tag{2.25}$$

The airspeed ($\bar{V}_\infty$) is given by the following expression:

$$\bar{V}_\infty = \bar{V}_w - \bar{V}_k = \bar{V}_w - (\bar{V}_{cg} + \bar{\omega} \times \bar{R}) \tag{2.26}$$

where $\bar{V}_w$ is the wind speed, $\bar{V}_{cg}$ is the velocity of the CG and $\bar{\omega} \times \bar{R}$ the velocity due to the rotations of the CG, equal to zero on the CG. The modulus of the airspeed (V) is given by:

$$V = \sqrt{u^2 + v^2 + w^2} \tag{2.27}$$

Finally, according to the geometry of the system, the angle of attack (α), the side-slip angle (β) and the path angle (γ) can be calculated by using the following equations:

$$\alpha = \arctan\left(\frac{w}{u}\right) \tag{2.28}$$

$$\beta = \arcsin\left(\frac{v}{V}\right) \tag{2.29}$$

$$\gamma = \arctan\left(\frac{\dot{z}}{\dot{x}}\right) \tag{2.30}$$

2.3.1 Apparent Mass Effect

For a light vehicle as a parafoil, the apparent mass has a strong effect on its dynamic behaviour. This effect occurs in all moving bodies immersed in a fluid, setting the fluid itself into motion and consequently creating an additional field of fluid momentum and energy surrounding the body. This volume of air that surrounds the canopy and moves with it makes it seem much heavier and increases the velocity of the system. When the lifting surface is notably separated from the payload, this effect becomes more significant due to the distance between the apparent mass center and the CG of the system, originating large apparent moments of inertia. These terms are obtained by deriving the kinetic energy of the fluid (T) as shown in Eq. 2.31 [24] [25]:

$$2T = A\tilde{u}^2 + B\tilde{v}^2 + C\tilde{w}^2 + P\tilde{p}^2 + Q\tilde{q}^2 + R\tilde{r}^2 + 2H(\tilde{v}\tilde{r} + \tilde{w}\tilde{q}) \tag{2.31}$$

in which A, B, C, P, Q, R and H are the coefficients for apparent mass, inertia and spanwise chamber, and $\tilde{u}$, $\tilde{v}$, $\tilde{w}$, $\tilde{p}$, $\tilde{q}$ and $\tilde{r}$ are the linear and angular aerodynamic velocities in the canopy axes. In [24], these terms were represented as in Figure 2.7.

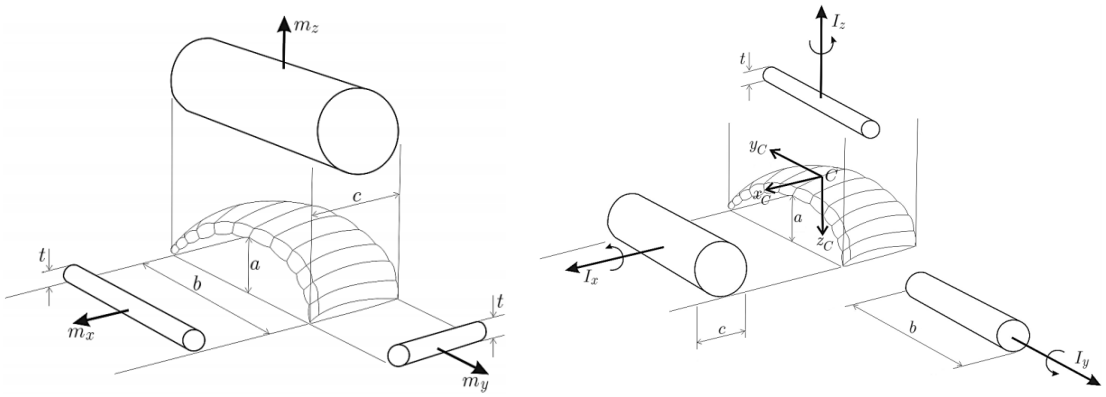

Figure 2.7: Apparent masses and inertias for translational and rotational motion [24].

The apparent mass center is the point where is experienced less resistance to rotational acceleration around the axis considered. It is necessary to define its position but, as stated by Barrows in [32], "*It is not possible to find a specific point in which the translational and rotational movements are decoupled*". As an approximation, this point has been assumed to be located in the aerodynamic center of the parafoil.

Then, considering a planar wing with an elliptical non-cambered cross-section in potential flow, [24] proposes the following expressions for calculating the apparent masses and inertias. They depend on the geometric parameters of the parafoil, including the thickness.

$$A = 0.666 \left(1 + \frac{8}{3}\left(\frac{a}{b}\right)^2\right) t^2 b \tag{2.32}$$

$$B = 0.267 \left[t^2 + 2a^2\left(1 - \left(\frac{t}{c}\right)^2\right)\right] c \tag{2.33}$$

$$C = 0.785 \left[1 + 2\left(\frac{a}{b}\right)^2\left(1 - \left(\frac{t}{c}\right)^2\right)\right]^{\frac{1}{2}} \frac{AR}{1+AR} b c^2 \tag{2.34}$$

$$P = 0.055 \frac{AR}{(1+AR)} b S_{ref}^2 \tag{2.35}$$

$$Q = 0.0308 \left[\frac{AR}{1+AR}\right] \left[1 + \frac{\pi}{6}(1+AR) AR \left(\frac{a}{b}\right)^2 \left(\frac{t}{c}\right)^2\right] c^3 S_{ref} \tag{2.36}$$

$$R = 0.0555 \left(1 + 8 \left(\frac{a}{b}\right)^2\right) b^3 t^2 \tag{2.37}$$

Considering the geometric values of the Snowflake and the Space Rider parafoils, the values of these coefficients obtained are shown in Table 2.3.

Snowflake				**Space Rider**			
A	0.0126	P	0.0433	A	12.5534	P	7144.3952
B	0.0061	Q	0.0062	B	4.6432	Q	444.0457
C	0.3357	R	0.0020	C	340.5810	R	319.3474

Table 2.3: Apparent mass coefficients.

Regarding the spanwise effect, in [16] this coefficient has been given a value of $H = 0.02$.

According to [16], the forces and moments due to the apparent mass and inertia can be calculated as follows:

$$\bar{F}_{AM} = -b2c^T \left(\bar{\bar{I}}_{AM} \begin{pmatrix} \dot{\tilde{u}} \\ \dot{\tilde{v}} \\ \dot{\tilde{w}} \end{pmatrix} + S^C_\omega \times \bar{\bar{I}}_{AM} \begin{pmatrix} \tilde{u} \\ \tilde{v} \\ \tilde{w} \end{pmatrix} \right) \tag{2.38}$$

$$\bar{G}_{AM} = -b2c^T \left(\bar{\bar{I}}_{AI} \begin{pmatrix} \dot{\tilde{p}} \\ \dot{\tilde{q}} \\ \dot{\tilde{r}} \end{pmatrix} + S^C_\omega \times \bar{\bar{I}}_{AI} \right) \tag{2.39}$$

where S^C_ω is the cross-product matrix of the angular velocities expressed in the canopy axes, and $\bar{\bar{I}}_{AM}$, $\bar{\bar{I}}_{AI}$ and $\bar{\bar{I}}_H$ are:

$$\bar{\bar{I}}_{AM} = \begin{bmatrix} A & 0 & 0 \\ 0 & B & 0 \\ 0 & 0 & C \end{bmatrix} \qquad \bar{\bar{I}}_{AI} = \begin{bmatrix} P & 0 & 0 \\ 0 & Q & 0 \\ 0 & 0 & R \end{bmatrix} \qquad \bar{\bar{I}}_H = \begin{bmatrix} 0 & H & 0 \\ H & 0 & 0 \\ 0 & 0 & 0 \end{bmatrix} \tag{2.40}$$

By developing the Eq. 2.38 and 2.39 according to [16], the following equations are finally obtained for the force and the moments due to the effect of the apparent mass.

$$\bar{F}_{AM} = -b2c^T S_\omega^C \times \left(\bar{\bar{I}}_{AM} \begin{pmatrix} \tilde{u} \\ \tilde{v} \\ \tilde{w} \end{pmatrix} \right) - \bar{\bar{I}}'_{AM} S_\omega^B \times i2b\overline{V}_w \tag{2.41}$$

$$\bar{G}_{AM} = -S_{CG.M}^B \times b2c^T S_\omega^C \times \left(\bar{\bar{I}}_{AM} \begin{pmatrix} \tilde{u} \\ \tilde{v} \\ \tilde{w} \end{pmatrix} \right) + b2c^T \left(S_\omega^C \times \bar{\bar{I}}_{AM} \right) \begin{pmatrix} \tilde{p} \\ \tilde{q} \\ \tilde{r} \end{pmatrix} - \left(S_{CG.M}^B \times \bar{\bar{I}}'_{AM} \right) S_\omega^B \times i2b\overline{V}_w \tag{2.42}$$

where it is considered the following assumption:

$$\bar{\bar{I}}'_x = b2c^T \cdot \bar{\bar{I}}_x \cdot b2c \tag{2.43}$$

These final equations are added to the rest of the forces and moments of the system according to Eq. 2.20 and 2.21. The inertias of the apparent mass must also be included into the total inertia of the system.

2.4 GPSim

The GPSim simulator is divided in different parts. First, the initialization of the input data is performed according to the following user-defined files:

- geometry.dat: Introduces the geometry of the parafoil. It also contains the values required for the discretization of the canopy in order to deal with the Horseshoe Vortex Method and the position of the payload CG and the apparent mass centre.
- configuration.dat: Contains the initial values for the CG and wind and the angles of the canopy, the initial position and target and the value of the time step for the loop.
- inertia.dat: Includes the moments of inertia of the parachute and its weight.
- GNC.dat: Provides the parameters used by the PID control system.

Then, the coordinates of the necessary points are calculated according to the entered geometry of the system. The descent boundary conditions are also initialized and the initial forces and moments of the system are calculated. The latter includes the weight and inertia of the parachute and the payload, the aerodynamics of the system and the effects of the apparent mass.

The integrator program simulates the trajectory, solving the equations of motion and, consequently, the state of the system during the descent. The CNG control system, discussed in Chapter 4, analyzes the trajectory and attitude of the system in order to be able to modify the control surfaces and the necessary parameters during the navigation.

The flow chart in Figure 2.8 shows the main structure of the GPSim flight simulator. The Matlab® functions implemented throughout the program are detailed and described below.

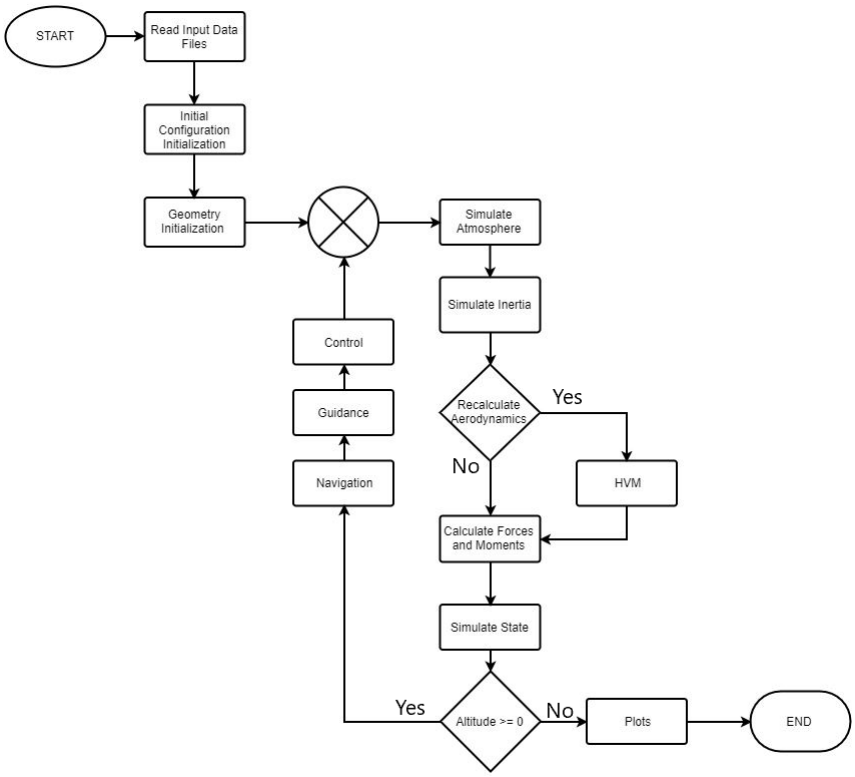

Figure 2.8: Flow chart of the GPSim.

- **addmass**: Calculates the added mass at each time step of the loop.
- **apparent_mass_matrices**: Calculates the apparent mass matrices according to the geometrical input values of the system.
- **configuration**: Reads and simulates the initial configuration of the system.
- **COORDINATES**: Calculates the geometric points and parameters of the parafoil. It includes the bound vortex points, the control points and the chord and surface distribution of each horseshoe vortex element. This function is included into the "geometry" function.
- **cross_product_matrix**: Cross product matrix function.

- **EULER**: Integrator solver that solves that manages the state of the system at each time step of the loop. It is included into the "simulate_state" function.
- **geometry**: Reads and simulates the geometry of the system.
- **GNC**: Navigation, Guidance and Control system.
- **GNC initialization**: Reads and initializes the GNC parameters introduced by the user.
- **GPSim**: Main function of the GPSim flight simulator. The target point coordinates and the initial height of the system can be introduced in its header.
- **gravity**: Simulates the gravity at each time step of the loop.
- **HVM**: Aerodynamic solver which applies the HVM. It is executed according to a tolerance angle introduced for the values of the angles α, roll, pitch and yaw.
- **inertia_initialization**: Initializes the inertia of the system.
- **inertia_track**: Determines the relative position of the system from the target point. It is included into the "GNC" function.
- **matrices_definition**: Calculates the transformation matrices for the different axes.
- **payload_loads_contribution**: Calculates the forces and moments due to the payload.
- **plots**: Final plots and results of the descent.
- **simulate_apparent_mass**: Calculates the forces and moments due to the apparent mass.
- **simulate_atmosphere**: Simulates the air density at each time step of the loop.
- **simulate_inertia**: Calculates the total inertia of the system.
- **simulate_state**: Simulates the state of the system. Includes the dynamic integrator solver. It is the first step of the loop and is run if the altitude is higher than 0. If not, the program simulation ends after plotting the results obtained.
- **state_derivatives**: Solves the dynamic equations of the system. It is included into the "EULER" function.
- **vortxl**: Calculates the induced velocities and downwash into the "HVM" function according to the Biot-Savart law.

2.4.1 Time Integrator

In order to simulate the trajectory and obtain the different states of the dynamic parameters, the equations of motion are solved numerically by using three different explicit methodologies for time integration: Euler, Runge Kutta of 2nd order and Runge Kutta of 4th order.

After analyzing the operation of the three methods, the one chosen for the integration of the equations of motion and the numerical solvers has been the Euler method. This decision has been made because this method gives acceptable results and requires fewer calculations in the loop, thus providing a faster simulation. This first order explicit integrator is defined by the following equation:

$$X_e[i] = X_e[i-1] + \Delta X_e \cdot \Delta t \tag{2.44}$$

where X_e is the state vector, ΔX_e is the rate of variation of the state vector, and Δt is the time increment or time step. The vector X_e includes the position, linear and angular velocities and the roll, pitch and yaw angles of the system, as shown below:

$$X_e = [x \quad y \quad z \quad u \quad v \quad w \quad p \quad q \quad r \quad \phi \quad \theta \quad \psi] \tag{2.45}$$

Analyzing the maximum time step increment admissible by the explicit integrator method, in order to provide acceptable descent results, it has been proved that its value must have an order of magnitude of around $10^{-3}s$.

For the main purpose of increasing efficiency, in [6] was decided to avoid recalculation of the aerodynamics at each time step (each call to the aerodynamic solver involves the assembly and solution of a linear $n \times n$ equation system). The condition to recalculate is that neither the angle rotated by the system in any of the axes nor the variation of the angle of attack from the last call of the aerodynamic solver must be greater than a defined tolerance. This condition allows to reduce considerably the number of calls to the aerodynamic code, reducing the computational cost with no significant variation of the accuracy in the results. Otherwise, the aerodynamic code would be called thousands of times during the simulation, significantly increasing the time required to obtain the final results.

2.4.2 Preliminary Assessment

In order to probe the correct functioning of the dynamic code, different descent situations have been simulated for the Space Rider and the Snowflake systems.

The following test shows the study of a parabolic shot of the system, considering only its mass. The effects of the apparent mass and the rotations due to the payload location with respect to the CG have not been considered. The simulation starts with the Space Rider facing North with an horizontal velocity v_x of $25m/s$. Figure 2.9 shows the path followed by the system:

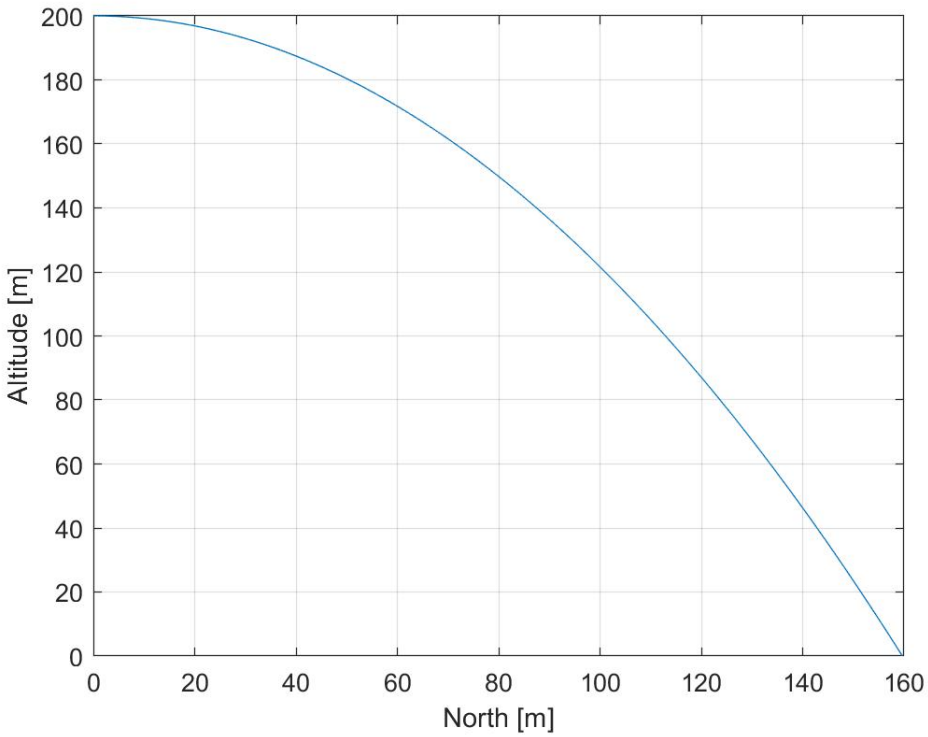

Figure 2.9: Space Rider parabolic descent.

The graph obtained describe a parabolic shot. To check if the simulation provides good results with the time step defined ($\Delta t = 0.001s$), the analytical result of the parabolic shot is used:

$$y = y_0 + v_{0y}t - \frac{1}{2}gt^2 \longrightarrow t = \sqrt{\frac{y \cdot 2}{g}} = 6.327s \tag{2.46}$$

$$x = x_0 + v_{0x}t = 158.187m \tag{2.47}$$

Then, Figure 2.10 shows the variation in time of the CG speed:

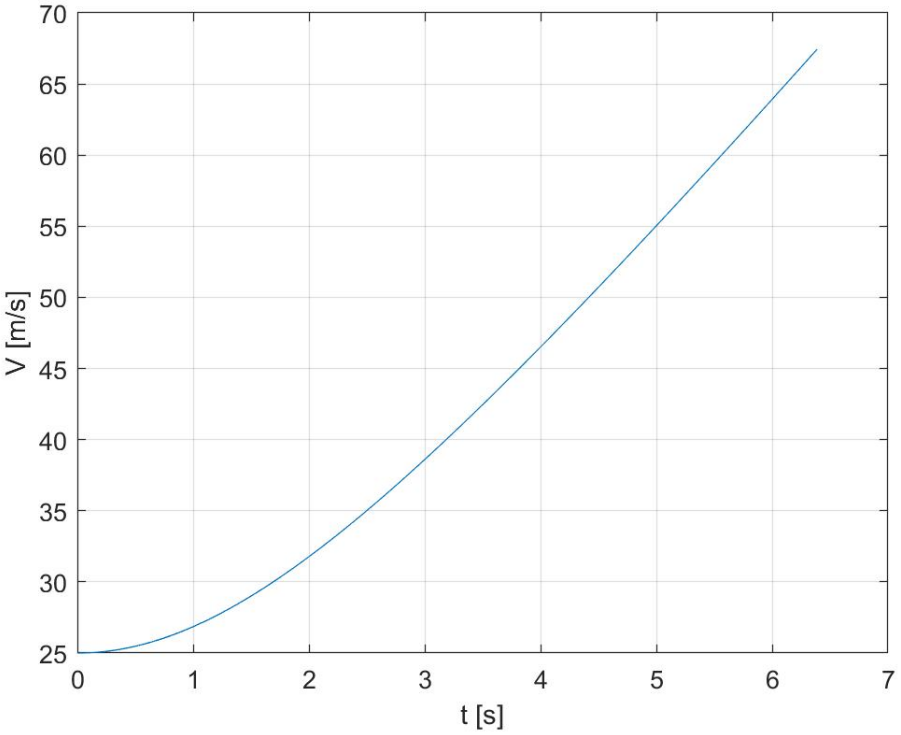

Figure 2.10: Variation of the CG speed.

Now, the CG speed when touching the ground is calculated analytically as follows:

$$v_y = v_{y0} + gt = 62.068 m/s \tag{2.48}$$

$$V = \sqrt{v_x^2 + v_y^2} = 66.9135 m/s \tag{2.49}$$

The values obtained by the simulation are $t = 6.387s$, $x = 159.700m$ and $V = 67.446m/s$. It means that the simulation brings results very similar to the exact ones with a time step that does not involve a high computational cost during the loop. The small difference between these results is probably due to the consideration of gravity. In the analytical calculation the constant value at sea level is considered while in the program it is implemented in the integrator time and it varies according to the height with a correction factor, mentioned in Section 2.2.3. In addition, the integration using the Euler method also has a certain error, since it is a first order method.

On the other hand, the variations in time of the angles of the system are shown in Figure 2.11:

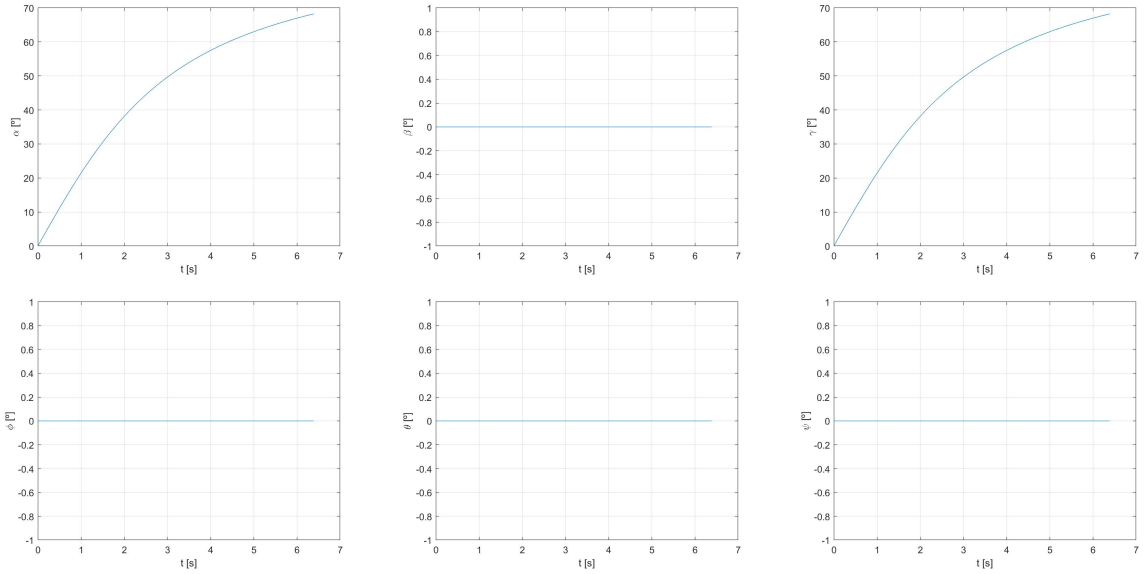

Figure 2.11: Space Rider descent angles.

As it is expected, there are no rotations of the system and thus the roll, pitch and yaw angles are equal to zero, as there is the side-slip angle because the system is always facing North. On the other hand, the airspeed direction of the system varies along the path, it descends, reason why positive values of the AoA and the path angle appear.

In the case of the Snowflake model, being a parabolic shot similar results have been obtained (these are not reported here).

Chapter 3

Aerodynamic Model

This chapter deals with the calculation of the aerodynamic forces and moments of the system. First, the basic aerodynamic equations for the parachute and the vehicle are shown. Then, according to the Lifting Line Theory, it is proposed the resolution of the parachute aerodynamic forces and moments by using the Horseshoe Vortex Method. Finally, the results obtained for the Space Rider are validated comparing them with other works and references.

3.1 Parafoil Aerodynamics

In this section, a typical parametric model for calculating aerodynamic forces and moments is described. As shown in Figure 3.1, the aerodynamic forces and moments are calculated in the wind axes and then transformed to the body axes in order to join the Eq. 2.20 and 2.21. On the one hand, the lift coefficient (C_L) is computed as:

$$C_L = C_{L\alpha}(\alpha - \alpha_{L0}) = C_{L0} + C_{L\alpha}\alpha \tag{3.1}$$

where $C_{L\alpha}$ is the lift curve slope, q the dynamic pressure and α_{L0} is the zero lift angle of attack.

On the other hand, the Drag coefficient (C_D) is given by the following equation:

$$C_D = C_{DO} + C_{D\alpha}\alpha^2 = C_{DO} + kC_L^2 \tag{3.2}$$

where C_{DO} is the parasite drag and $C_{D\alpha}\alpha$ or kC_L^2 the induced drag (C_{Di}). C_{DO} and k are characteristic values of the parafoil.

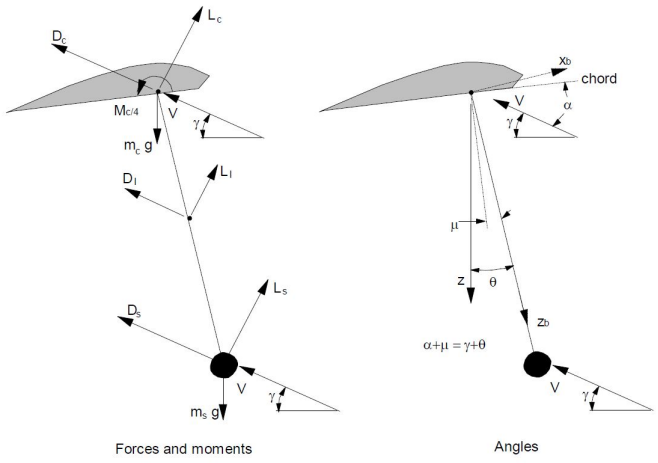

Figure 3.1: Forces, moments and angles in the Wing Axes [23].

The suspension lines also generate a considerable drag, while the lift can be neglected, due to the direction in which they are oriented. As it is proposed in [21], this drag is given by:

$$C_{D_l} = \frac{num \cdot R \cdot d \cdot \cos\alpha^3}{S} \tag{3.3}$$

where num is the number of connecting lines and d their diameter. According to [23], these constant parameters may have for the Space Rider due to its surface a value of approximately $num = 90$ and $d = 2.5mm$.

The vehicle drag coefficient $C_{D_{PL}}$ depends on its shape and the reference surface (S_{PL}). From experimental data, a value of $C_{D_{PL}} = 0.185$ is obtained.

The Lateral force coefficient (C_Y) depends on the Side-slip Angle and is computed as:

$$C_Y = C_{Y_\beta}\beta \tag{3.4}$$

Then, the coefficients for the aerodynamic moments are given by the following expressions:

$$C_m = C_{m_q} q\frac{c}{2V} + C_{m_0} + C_{m_\alpha}\alpha \tag{3.5}$$

$$C_n = C_{n_\beta}\beta + C_{n_p} p\frac{b}{2V} + C_{n_r} r\frac{b}{2V} \tag{3.6}$$

$$C_l = C_{l_\beta}\beta + C_{l_p} p\frac{b}{2V} + C_{l_r} r\frac{b}{2V} \tag{3.7}$$

Finally, the aerodynamic forces and moments of the canopy and the Drag force of the payload are passed to the body axes as required in the Eq. 2.20 and 2.21 as follows:

$$\bar{F}_A = \frac{1}{2}\rho V^2 S[w2b] \begin{bmatrix} C_{D0} + C_{D\alpha}\alpha^2 + C_{Dl} \\ C_{Y_\beta}\beta \\ C_{L0} + C_{L\alpha}\alpha \end{bmatrix} \tag{3.8}$$

$$\bar{F}_{PL} = \frac{1}{2}\rho V^2 S_{PL}[w2b] \begin{bmatrix} C_{D_{PL}} \\ 0 \\ 0 \end{bmatrix} \tag{3.9}$$

$$\bar{G}_A = \frac{1}{2}\rho V^2 S[w2b] \begin{bmatrix} C_{m_q} q\frac{c}{2V} + C_{m_0} + C_{m_\alpha}\alpha \\ C_{n_\beta}\beta + C_{n_p} p\frac{b}{2V} + C_{n_r} r\frac{b}{2V} \\ C_{l_\beta}\beta + C_{l_p} p\frac{b}{2V} + C_{l_r} r\frac{b}{2V} \end{bmatrix} \tag{3.10}$$

$$\tag{3.11}$$

According to the thin airfoil theory, the angle of attack must be small so that the viscous forces can be neglected. The same happens for the deflection of the control surfaces, they must have relatively small values. Regarding the effects of the control surfaces deflection, a positive deflection (δ) implies a decrease in the α_{L0}. This supposes an increase of the lift for the same value of α but a reduction of the α_{stall}. Thus, a proportional increment in C_L, C_{Di} and C_m also appears, since they depend on the angle of attack. The incremental values of these forces and moments are obtained experimentally or numerically. In the GPSim simulator the coefficients of this parametric model are computed in the loop.

In case of a symmetric deflection of the control surfaces, the system remain stable because the lift distribution remains symmetrical on both semi-spans. If there is a small difference in the values of δ between both ailerons, the system will turn to the direction of the less deflected aileron because the other one performs a lift gain that elevates its semi-span. If it has a high value, it turns to the side where the aileron is most deflected because the increase in the drag force is greater than that of the lift force.

3.1.1 Lifting Line Theory for Gliding Parachutes

As for rigid wings, the Lifting Line Theory (LLT) can also be used to estimate the lift and drag coefficients of a gliding parachute. However, this theory is effective for high aspect ratio values, greater than 5, and some corrections should be made for low aspect ratio effects, as occurs with the Space Rider parafoil (AR=3). Lingard proposes in [23] the considerations and modifications to the LLT that will be explained in this section.

In case of wings with high aspect ratios ($AR > 5$), the C_L has a linear behaviour with respect to α and is obtained as:

$$C_L = C_{L_\alpha}(\alpha - \alpha_{L0}) \tag{3.12}$$

where α_{L0} is the value of the AoA for a lift force equal to zero and C_{L_α} is the wing's lift slope, obtained by the following equation:

$$C_{L_\alpha} = \frac{\pi C_{l_\alpha} AR}{\pi AR + C_{l_\alpha}(1+\tau)} \tag{3.13}$$

This expression does not fit gliding parachutes with lower aspect ratios. It is required to add a non-linear term and make a correction to the lift slope by means of a K factor:

$$C_{L_{gliding}} = \left(C'_{L_\alpha}(\alpha - \alpha_{L0})\right)_{linear} + (\Delta C_L)_{nonlinear} \tag{3.14}$$

$$C'_{l_\alpha} = C_{l_\alpha} K \tag{3.15}$$

$$K = \frac{2\pi AR}{C_{l_\alpha}} \tanh\left(\frac{C_{l_\alpha}}{2\pi AR}\right) \tag{3.16}$$

Then, it is possible to rewrite Eq. 3.13 with the new considerations:

$$C'_{L_\alpha} = \frac{\pi C'_{l_\alpha} AR}{\pi AR + C'_{l_\alpha}(1+\tau)} \tag{3.17}$$

where τ is a small positive factor that increases the induced angle of incidence over that for the minimum case of elliptic loading. According to [23], this value depends on AR as it is shown in the curve in Figure 3.2:

The linear aspect of Eq. 3.14 can be calculated by using Eq. 3.17. Otherwise, the lift increment caused by the non linear aspect is estimated as follows:

$$\Delta C_L = K_1 sin^2(\alpha - \alpha_{L0}) cos(\alpha - \alpha_{L0}) \tag{3.18}$$

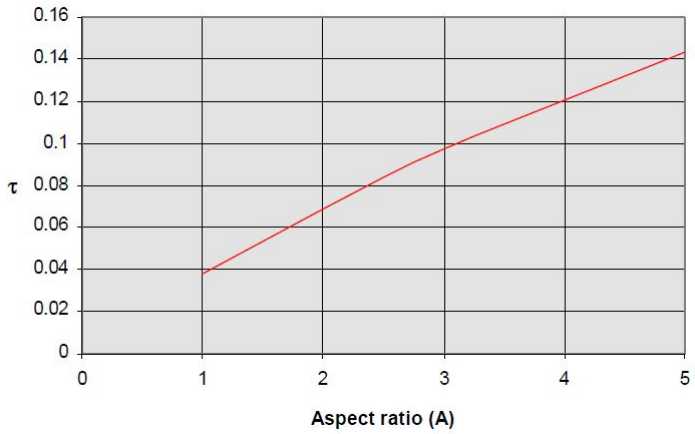

Figure 3.2: Tau vs Aspect Ratio [23].

The K_1 can be calculated as $K_1 = 3.33 - 1.33AR$ for $1 < AR < 2.5$ and considered equal to zero for $AR > 2.5$. Then, the C_L is given by:

$$C_L = C'_{L_\alpha}(\alpha - \alpha_{L0}) + K_1 sin^2(\alpha - \alpha_{L0})cos(\alpha - \alpha_{L0}) \tag{3.19}$$

The C_L can also vary according to the shape of the canopy. The arc-anhedral (γ) effect modifies the linear part of the coefficient as follows [23]:

$$C_L = C_{L_{\gamma=0}} cos^2(\gamma) \tag{3.20}$$

where according to the parafoil geometry, the value of γ is obtained as:

$$\gamma = \frac{\varepsilon}{2} = \frac{b}{4R} \tag{3.21}$$

Finally, introducing this consideration in Eq. 3.19, it is obtained the final equation:

$$C_L = C'_{L_\alpha}(\alpha - \alpha_{L0})cos^2(\gamma) + K_1 sin^2(\alpha - \alpha_{L0})cos(\alpha - \alpha_{L0}) \tag{3.22}$$

On the other hand, regarding the drag coefficient, as mentioned in the previous section it is composed by the sum of the parasite drag (C_{D_p}) and the induced drag (C_{D_i}). The first one is the contribution of the profile drag (C_{d_p}) along the span, given by the following equation [6] [23]:

$$C_{D_p} = \frac{1}{S_{ref}} \int_{-\frac{b}{2}}^{\frac{b}{2}} C_{d_p}(C_l(y))c(y)dy \tag{3.23}$$

The induced drag, or drag due to lift, according to the LLT can be calculated as:

$$C_{D_i} = \frac{C_L^2}{\pi AR\epsilon} = \frac{C_L^2(1+\delta)}{\pi AR} \tag{3.24}$$

where ϵ and δ are geometric parameters of the canopy, which is considered as an elliptical shape. The latter depends on the AR of the parafoil, as shown in Figure 3.3:

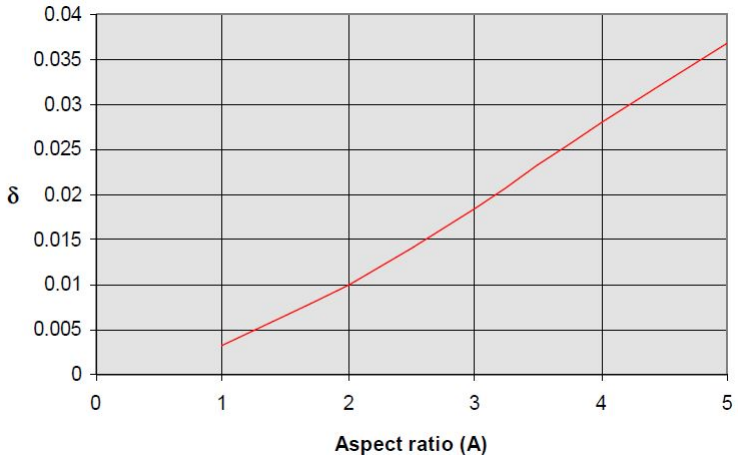

Figure 3.3: Delta VS AR [23].

Regarding the corrections made to the C_L, it also affects the C_D coefficient due to the induced term. In this way, a new non-linear aspect appears, as shown below:

$$\Delta C_D = K_1 sin^3(\alpha - \alpha_{L0}) \tag{3.25}$$

Finally, the C_D for gliding parachutes is calculated by the following equation:

$$C_D = C_{D_p} + \frac{C_{L_C}^2}{\pi AR\epsilon} + K_1 sin^3(\alpha - \alpha_{L0}) \tag{3.26}$$

where C_{L_C} is the circulation lift coefficient, given by:

$$C_{L_C} = C'_{L_\alpha}(\alpha - \alpha_{L0}) \tag{3.27}$$

It should be noted that this C_{L_C} does not consider the non-linear lift increment given by Eq. 3.18, but in Eq. 3.26 the non-linearity operates by the third term.

Taking into account that the system also deals with a drag due to the suspended lines, as mentioned before, the total drag coefficient of the entire system results:

$$C_D = C_{D_l} + C_{D_p} + \frac{C_{L_C}^2}{\pi AR\epsilon} + K_1 sin^3(\alpha - \alpha_{L0}) \tag{3.28}$$

Regarding the value of α_{L0}, it can be obtained from reported experimental data. The parafoil's cross-sectional wing shape and characteristics show great similarities to the Clark-Y parafoil airfoil, an adaptation of the Clark-Y airfoil model for gliding parachutes in which the effect of air intake is taken into account. This consideration has already been used in other works for various prototypes of gliding parachutes, as in [21]. According to Lingard in [23], the α_{L0} must have a value of approximately -7^o, which is adopted during the development of the aerodynamic solver.

Finally, comparisons between experimental and analytical results obtained by Lingard in [23] for different Aspect Ratio gliding parachute models are shown in Figure 3.4. These results serve as an example to adjust the experimental coefficients required for simulation. Glouchtchenko's work [21] based on the results for the NASA X-38 model, taking it as a reference for the Space Rider prototype. This is relevant since this last mentioned work offers results for the descent of the Space Rider and is a good source to compare and trim the system in this work.

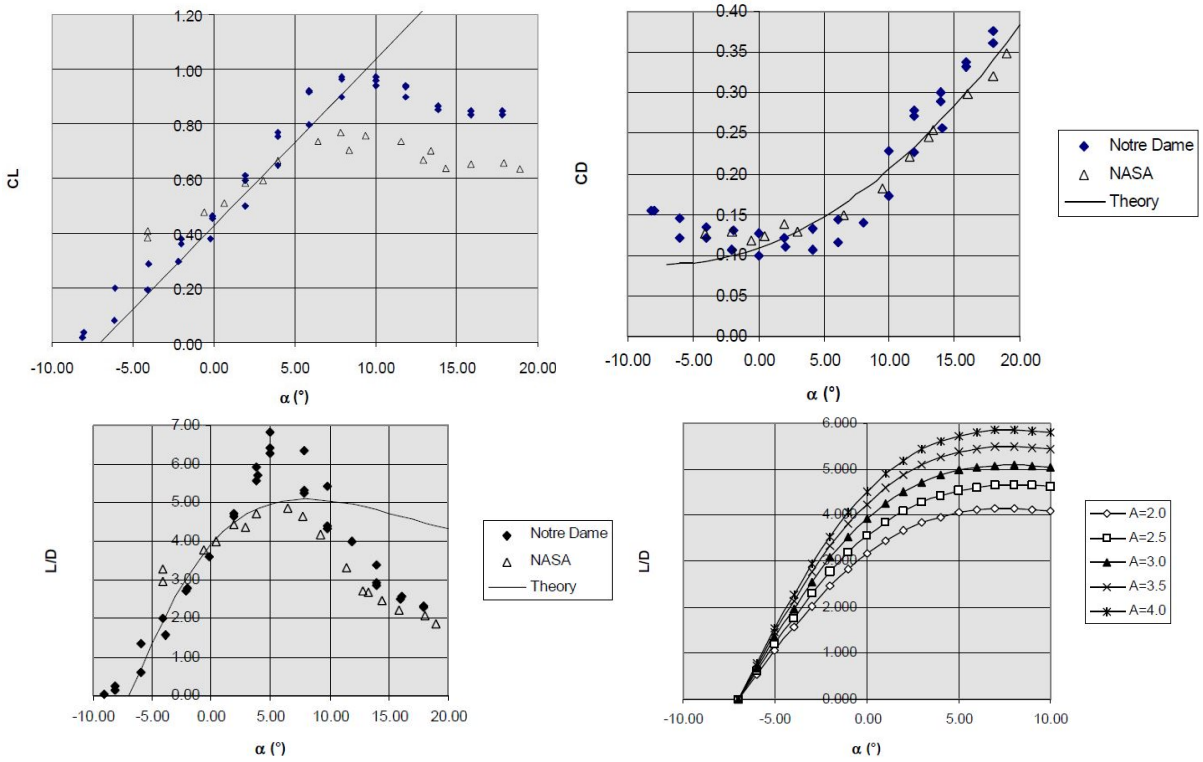

Figure 3.4: Reported aerodynamic coefficients values [23].

3.2 Horseshoe Vortex Method

This section introduces and develops the Horseshoe Vortex Method (HVM), which allows to solve numerically the Prandtl's lifting line problem. It allows to compute the lift, induced drag, moments and spanwise load distribution, considering the wing sweep, twist and the deflection of the control surfaces. This methodology is fast and simple, thus reducing significantly the computational costs of the program in comparison with other approaches such as the vortex lattice originally used in GPSim. It does not deal with the thickness effects and it is only applicable for thin wings, which is the case of the Space Rider parafoil [22] [33].

According to this method, the wing is discretized in N horseshoe vortex elements in the spanwise direction (y-axis).

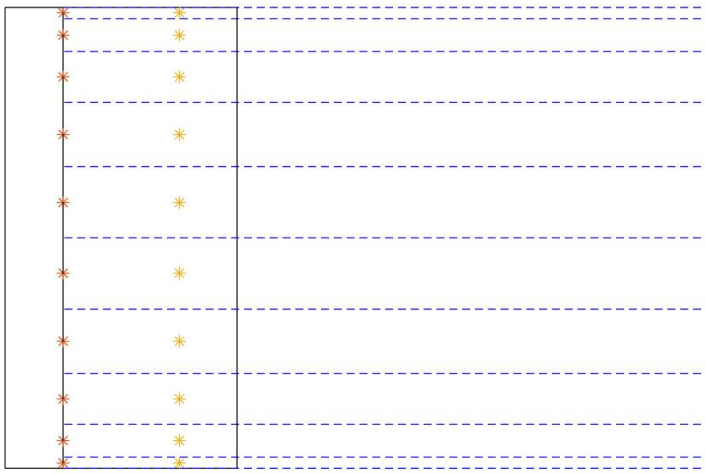

Figure 3.5: Horseshoe vortex elements.

The horseshoe vortex elements are defined by the points X_A^i, X_B^i, X_C^i and X_D^i. The vortex line segment from X_B to X_C is the bounded vortex, and the vortex lines from X_A to X_B and from X_C to X_D are the trailing vortices. The control point is the point where problem equations are calculated. According to Weisinger's approximation, this control point is located at the y-direction midpoint of the three quarters chord line. This distribution is shown in Figure 3.6:

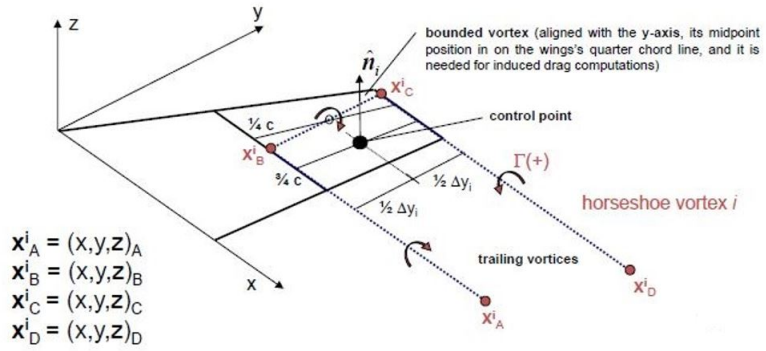

Figure 3.6: Horseshoe vortex element [33].

These vortex line elements satisfy the Laplace equation for potential flow. The boundary conditions applied to the control points result in the following expression:

$$\left[\left(u^i, v^i, w^i\right) + (U_\infty, V_\infty, W_\infty)\right] \hat{n}_i = 0 \tag{3.29}$$

where (u^i, v^i, w^i) are the induced velocities at each control point due to the vortices spanned along the wing and $\hat{n}_i$ is the normal vector in the control point with respect to the zero lift line of the section. The values of the velocities $U_\infty, V_\infty, W_\infty$ consider the reference velocity of the system and the angular velocities due to rotations at each control point of the discretization.

The induced velocities due to each vortex line are calculated by the Biot-Savart law as follows:

$$(u, v, w)_p = \frac{\Gamma}{4\pi}\left[\frac{r_0}{|r_1 \times r_2|}\left(\frac{r_1}{|r_1|} - \frac{r_2}{|r_2|}\right)\right]\frac{r_1 \times r_2}{|r_1 \times r_2|} \tag{3.30}$$

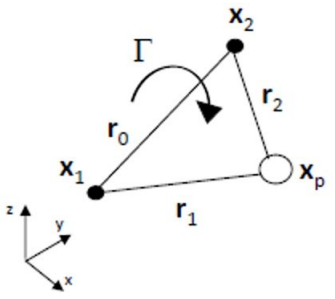

Figure 3.7: Biot-Savart law [22].

where r_0, r_1 and r_2 are the distances shown in Figure 3.7 and Γ the unknown circulation.

Then, it is obtained the following expression:

$$\left[\sum \Gamma_j \left(u^i, v^i, w^i\right)\right] \hat{n}_i = -\left(U_\infty, V_\infty, W_\infty\right) \hat{n}_i \tag{3.31}$$

The Eq. 3.31 can be solved for the unknown circulations, defining an influence coefficient A_{ij}:

$$A_{ij} = \left(u^i, v^i, w^i\right) \hat{n}_i \tag{3.32}$$

So, the Eq. 3.31 in matrix form can be expressed as:

$$\begin{bmatrix} a_{11} & \cdots & a_{1j} & \cdots & a_{1N} \\ \vdots & \ddots & \vdots & & \vdots \\ a_{i1} & \cdots & a_{ij} & \cdots & a_{iN} \\ \vdots & & \vdots & \ddots & \vdots \\ a_{N1} & \cdots & a_{Nj} & \cdots & a_{NN} \end{bmatrix} \begin{bmatrix} \Gamma_1 \\ \vdots \\ \Gamma_j \\ \vdots \\ \Gamma_N \end{bmatrix} = -\left(U_\infty, V_\infty, W_\infty\right) \begin{bmatrix} \hat{n}_1 \\ \vdots \\ \hat{n}_i \\ \vdots \\ \hat{n}_N \end{bmatrix} \tag{3.33}$$

The circulation at the control points can be calculated by solving this system. Now it is possible to find the contribution of the aerodynamic forces and moments at each bound vortex by applying the Kutta-Joukowski theorem.

$$\Delta \bar{F}_i = \rho(\bar{V}_i \times \Gamma_i \Delta \bar{x}_i) \tag{3.34}$$

where $\bar{V}_i$ is the sum of the kinematic and induced velocities, Γ_i is the circulation and $\Delta \bar{x}_i$ is the bound vortex vector.

The flow in HVM does not consider chordwise effects. Thus, the viscosity effects are neglected and the pressure contributions and free moment can not be calculated. For this reason, in order to calculate the airfoil parasite drag, the polar coefficients are entered as input data and it is calculated using the following expression, based on Eq. 3.23:

$$C_{D_p} = A_p C_l^2 + B_p C_l + C_p \tag{3.35}$$

where A_p, B_p and C_p are the coefficients of the airfoil drag. The C_l can be obtained by approximating the local force calculated in the z-axis of each bounded vortex as the lift of the airfoil. It means that the distribution of this coefficient along the wingspan can be calculated as:

$$C_l(y) \approx \frac{2F_Z(y)}{\rho \bar{V}_{ref,M}^2 S(y)} \tag{3.36}$$

being $S(y)$ the surface of each panel and $\bar{V}_{ref,M}$ the reference velocity in the Matlab axes, which gives directions to the Drag force in the three axes. Summing all the values obtained along the span, it is obtained the total C_{D_p} of the parafoil. The force exerted by this component is calculated as:

$$\bar{F}_p = \frac{1}{2}\rho \bar{V}_M^2 S C_{D_p} \hat{V}_{ref,M} \tag{3.37}$$

Finally, the total aerodynamic forces and moments are given by:

$$\bar{F} = \sum \Delta \bar{F}_i + \bar{F}_p \tag{3.38}$$

$$\bar{M}_{c/4} = -\sum \Delta \bar{F}_i (\bar{x}_i^{\Gamma} - \bar{x}_{c/4}) - \bar{F}_p \bar{x}_{c/4} \tag{3.39}$$

where $\bar{x}_i^{\Gamma}$ is the midpoint of the bounded vortex and $\bar{x}_{c/4}$ is the quarter chord point coordinates. The moment calculated must also add the contribution of C_{m0} of the airfoil.

As mentioned before, these values are obtained in the canopy axes and they must be transformed to the body axes, in order to join the rest of forces and moments of the system:

$$\bar{F}_A = b2c^T \bar{F} \tag{3.40}$$

$$\bar{G}_A = b2c^T \bar{M}_{c/4} + S_{CG.A}^B \times \bar{F}_A \tag{3.41}$$

3.3 Preliminary Assessment

In this section, the aerodynamic solver is verified. The main objective of this study is to obtain accurate approximations of the parachute aerodynamic coefficients with the minimum computational cost required. First, the optimal wing discretizations for the HVM is studied, as well as the geometric aspects of the Space Rider's parafoil that are required by this method. Then, the aerodynamic coefficients are calculated and compared with published empirical and analytical results. Finally, the results of a descent simulation are shown and presented.

3.3.1 Geometry and Discretization

The first step is analyze and determine a correct number of horseshoe panels for the discretization of the lifting line. This value is really important because it will define the accuracy and the computational cost of the aerodynamic solver, which will be called hundreds of times during the simulation. For this purpose, a study of the error in the aerodynamic coefficients vs. number of panels used is done for the Space Rider parachute. The results are shown in Figure 3.8:

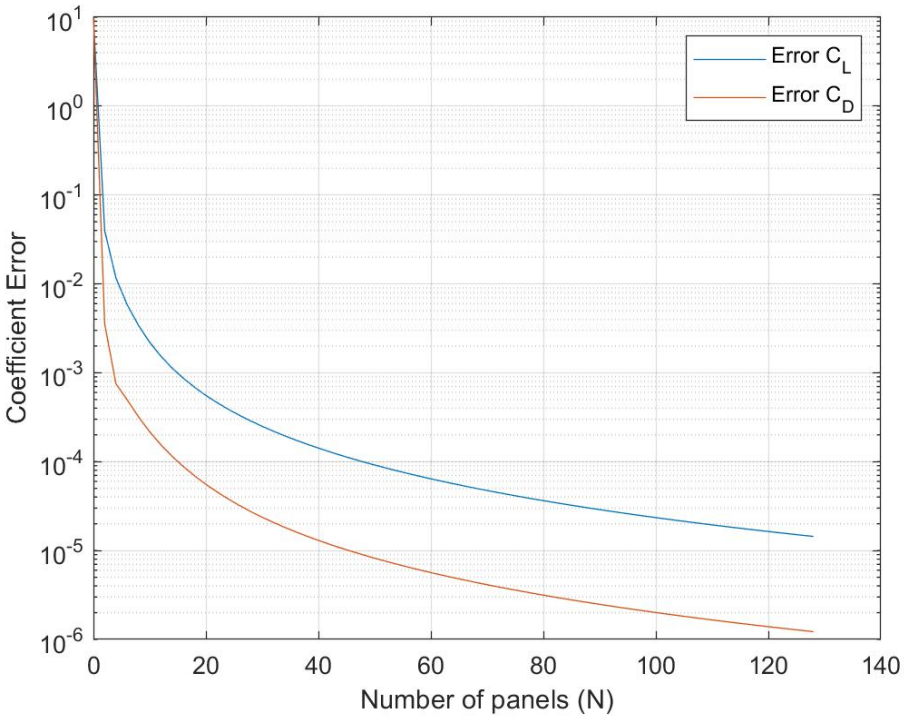

Figure 3.8: C_L and C_D error for different values of N.

Figure 4.1 shows the evolution of the error of C_L and C_D as N increases from 0 to 128 vortex elements, taking as initial reference a value of 10 for both coefficients. It has been considered an angle of attack of $\alpha = 5^o$, no deflection of the control surfaces and no rotations with respect to the CG. The graph obtained in Figure 3.8 shows that it is not required a large number of horseshoe vortices in order to obtain a good approach of the results by using the HVM. Table 3.8 shows the error of C_L and C_D for different values of N for the Space Rider parafoil:

N	C_L **error**	C_D **error**
$2^4 = 16$	8.6507e-4	8.7852e-5
$2^5 = 32$	2.2008e-4	2.0713e-5
$2^6 = 64$	5.6467e-5	4.9521e-6
$2^7 = 128$	1.4415e-5	1.2224e-6

Table 3.1: C_L and C_D error for different values of N.

Analyzing the results obtained, it is chosen $N = 64$. This value performs accurate approximations in the results and does not affect notably to the computational cost of the program.

Regarding the position of the points defined by each horseshoe vortex, the bounded vortex and control points, it depends on the geometry of the wing. Parafoils actually have a small sweep (Λ) and dihedral (γ) angle, so the position of these points would be structured as in Figure 3.9:

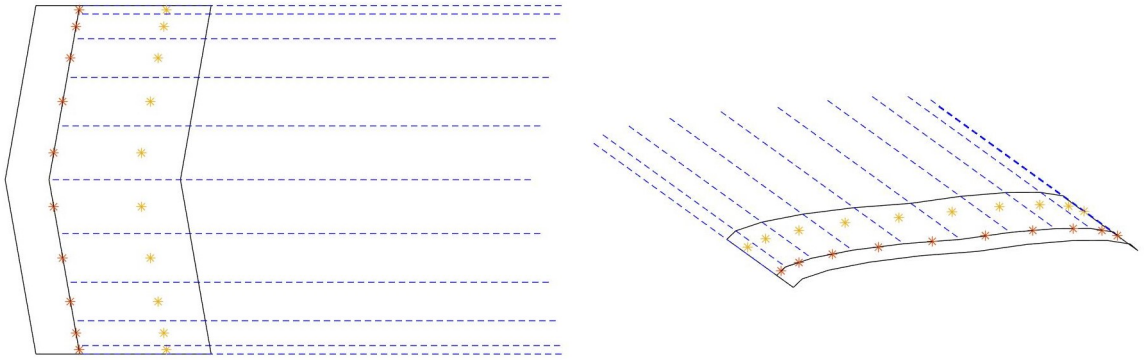

Figure 3.9: Discretization with sweep angle.

where the red points are the bounded vortex and the yellow ones the control points.

3.3.2 Aerodynamic Coefficients

This section presents the aerodynamic coefficients obtained for the Space Rider parafoil by using the HVM. These values have been calculated analytically by using the approaches proposed by Lingard [23] and Yakimenko [26]. Also, the results obtained have been compared with those presented by Glouchtchenko in [21] for the X-38 parafoil model coefficients. The aerodynamic coefficients obtained for the Space Rider parafoil are shown in Figure 3.10:

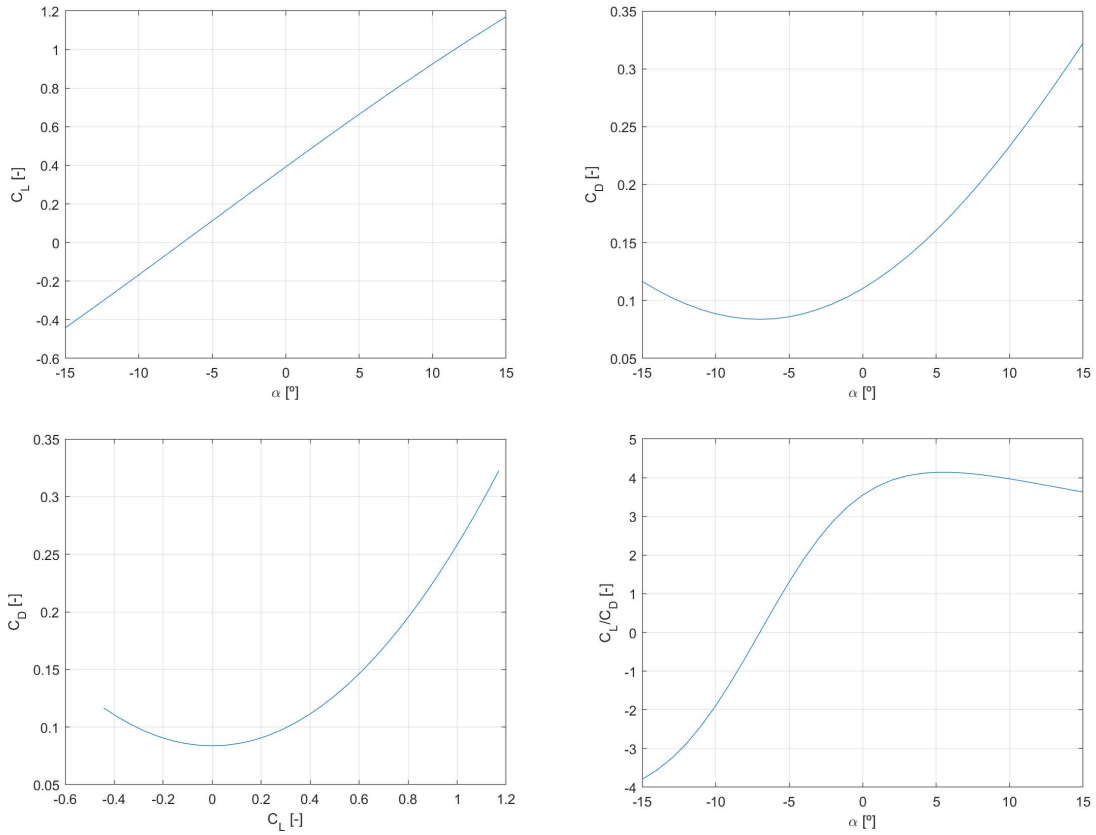

Figure 3.10: Aerodynamic coefficients of the Space Rider.

To obtain these results, the polar curve obtained with the HVM has been adjusted to the analytical results using the aforementioned equations, as shown in Figure 3.11. In section 3.1.1. it is mentioned that α_{L0} has a value of -7^o according to the Clark-Y parafoil airfoil approximation [23] [21]. The experimental drag polar coefficients obtained are: $C_{D0} = 0.084$, $k1 = 6 \cdot 10^{-5}$ and $k2 = 0.072$.

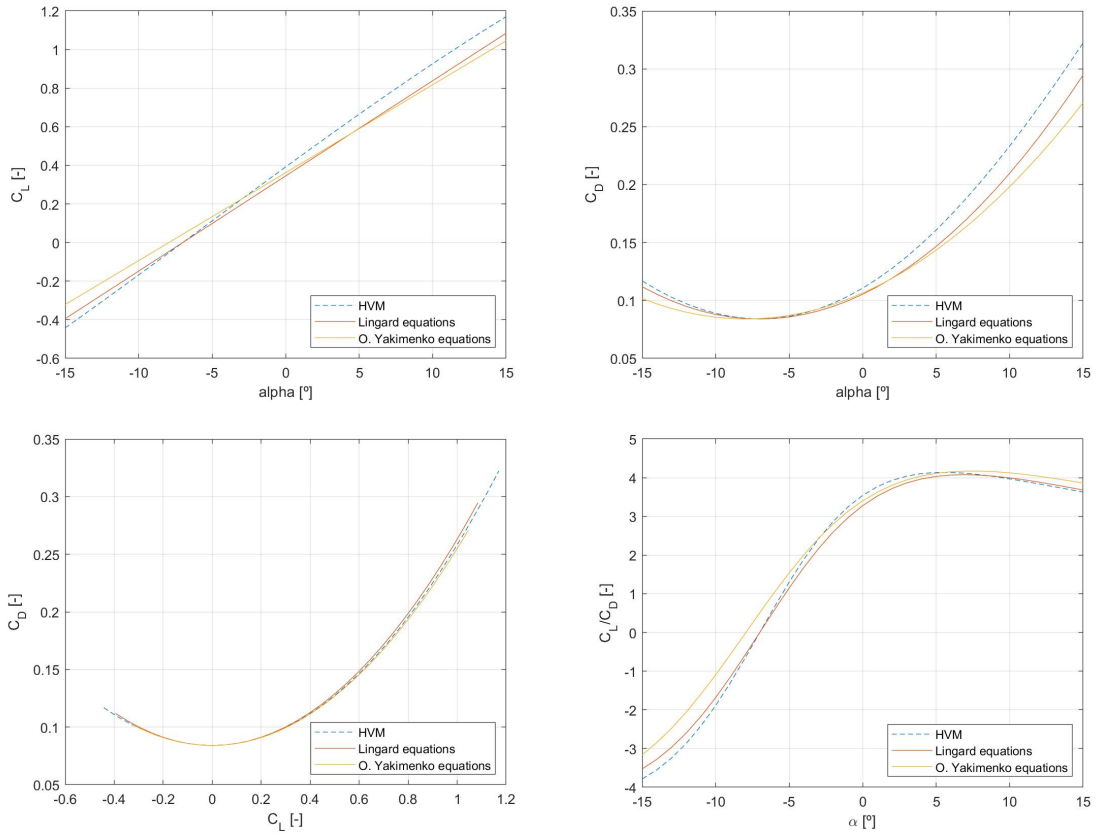

Figure 3.11: Comparison of HVM and theoretical-empirical estimations of the aerodynamic coefficients.

In the thesis of Glouchtchenko, it was also studied the descent of the Space Rider system. In this case, the aerodynamic coefficients were considered with the X-38 as a reference, due to its similarity. Moreover, Lingard also presents some publications made by NASA for the X-38 model, the ones shown previously in Figure 3.4. Figure 3.12 shows the results reported by Glouchtchenko for the X-38 model in the linear zone:

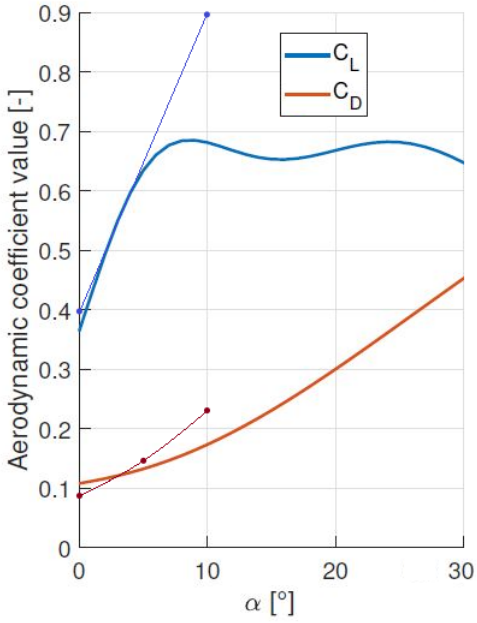

Figure 3.12: Reported aerodynamic coefficients of the X-38 parafoil [21].

Then, Table 3.2 shows some relevant parameters obtained for the different results presented:

	$C_{L\alpha}$ [-]	C_{D0} [-]	α_{L0} [°]
HVM	3.12	0.084	-7
Lingard equations	2.81	0.084	-7
Yakimenko equations	2.61	0.084	-8
X-38 (reported)	3.16	0.095	-6.5

Table 3.2: Aerodynamic parameters.

It can be considered that the solver meets its requirements since it provides quite accurate results to those obtained in other works and references, specially on the linear zone and for small values of the angle of attack, where the system must operate. Also, it can be seen how the Space Rider reaches an aerodynamic efficiency of 4, characteristic for parafoils with $AR = 3$ as stated by Lingard [23].

In order to evaluate the C_m, Figure 3.13 shows the variation of this coefficient obtained for the Space Rider (left) and the reported values for the X-38 in [21](right):

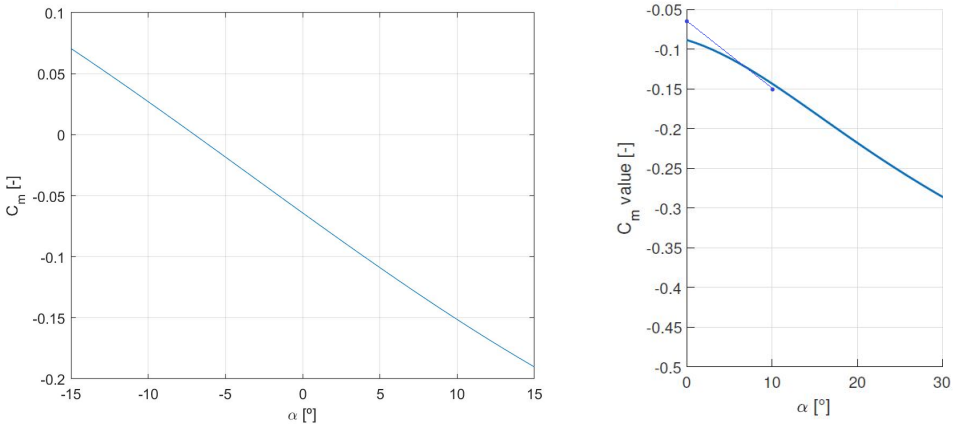

Figure 3.13: Cm slope of the Space Rider (left) and the reported X-38 (right) [21].

The $\partial C_m/\partial\alpha$ slope is negative, this fact guarantees the longitudinal stability of the system.

Then, Figure 3.14 shows the sections C_l distribution along the span for different α values:

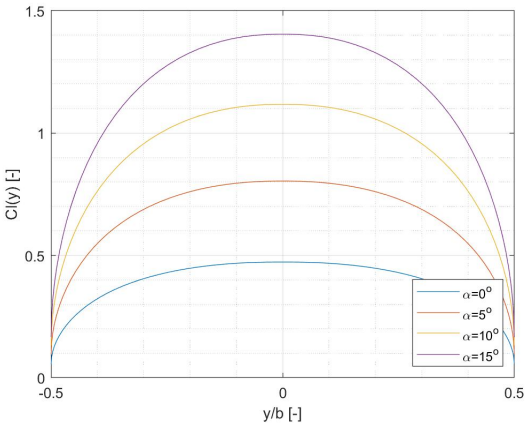

Figure 3.14: $C_l(y)$ distribution along the wing span.

According to the graphs shown in Figure 1, Figure 3.14 shows how as the α increases in the linear zone, the C_l distribution also increases and therefore, the total lift of the canopy does too. The highest value of C_l is located at the root chord and decreases in each semi-wing as it approaches to the tip chord, where its value is zero.

Finally, to check the proper operation of the control surfaces within the program, it is analyzed the behavior of the aerodynamic coefficients when deflecting them. As stated in the previous section, this methodology used does not allow high deflection angles. Figure 3.15 shows the graphs for different values between $\delta = \pm 10^o$:

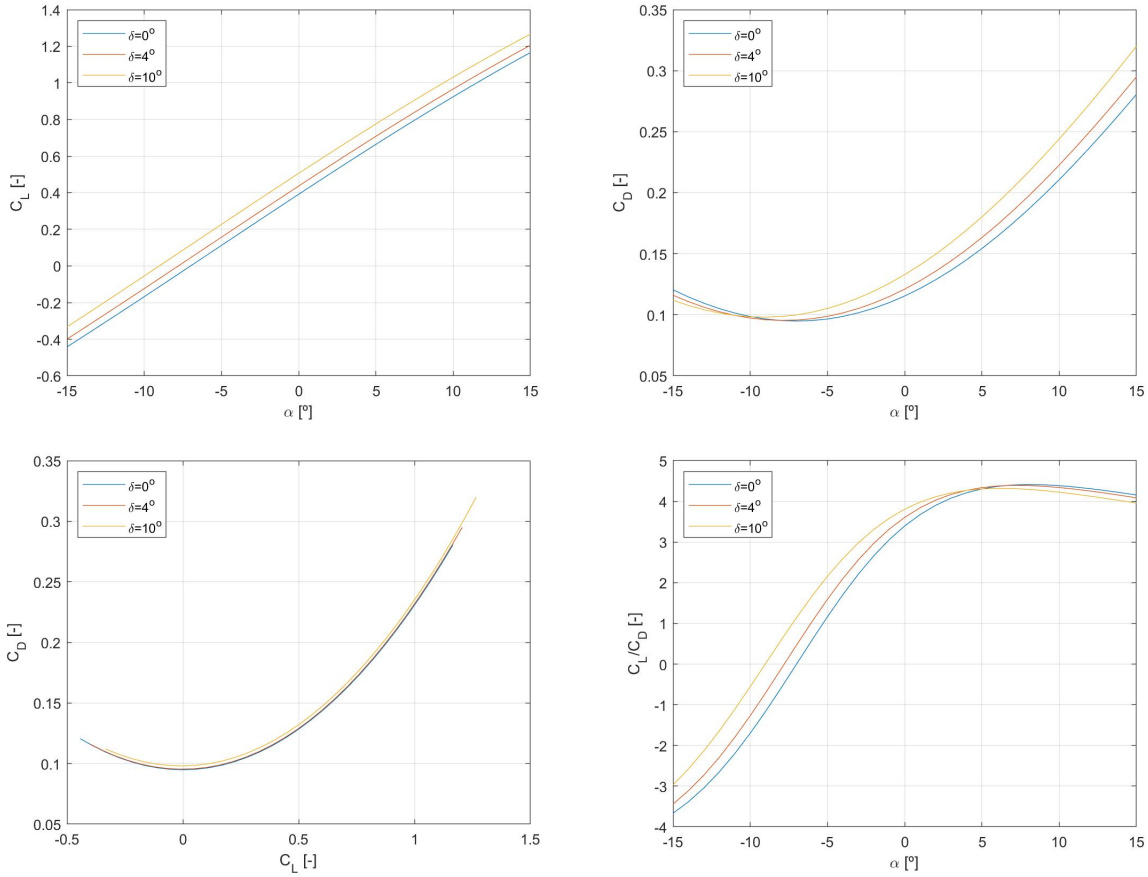

Figure 3.15: Lift and drag coefficients variation with aileron deflection.

As the aerodynamic theory establishes, by positively increasing the deflection of the flaps, both the C_L and the C_D increase. The graphs move to the left as δ increases (changes the angle of zero lift), obtaining higher values of the coefficients for the same value of the angle of attack. Consequently, α_{stall} decreases and C_{L0} increases, but the slopes remain equal. The ailerons are only allowed to deflect in the positive direction because of the the geometry of the parafoil, which only allows pulling with the suspension lines downwards.

3.3.3 Descent

In order to verify the proper functioning of the HVM, an initial test is presented for the Snowflake system (there are more references than for the Space Rider). The results are compared with those obtained in [6] by using the VLM. Table 3.3 shows the initial configuration values and Figure 3.16 the descent obtained (left) and those reported in [6](right).

Initial configuration parameters	
Initial linear velocity	[10,0,0] m/s
Initial angular velocity	[0,0,0] rad/s
Initial parafoil attitude	[0,0,0] rad
Initial altitude	200 m
Rigging angle	-12^o
Left/Right CS deflection	0º / 0º
Mass	2.37 kg

Table 3.3: Initial configuration parameters Snowflake.

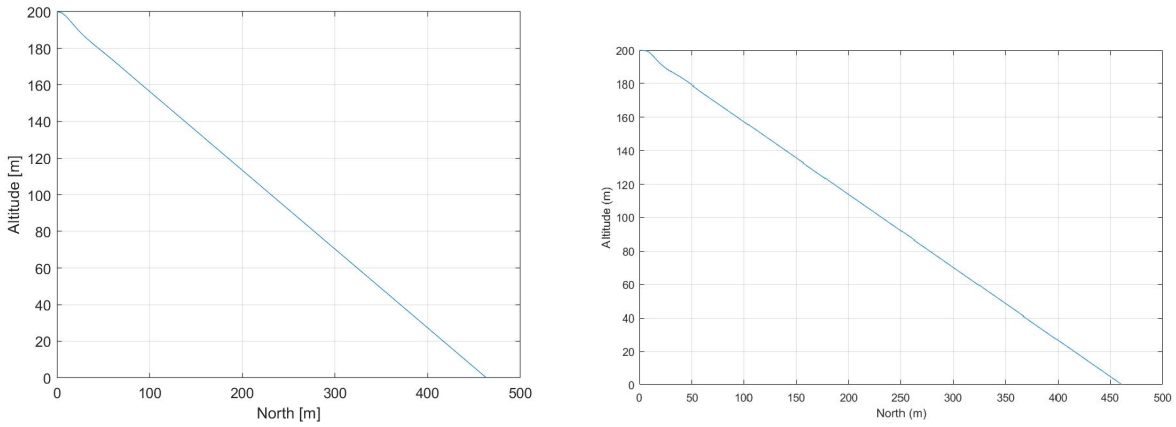

Figure 3.16: Snowflake descent with HVM (left) and reported VLM (right) [6].

The descent time is 43.587s, the distance traveled 463.342m and the final speed 11.592m/s. These results have been obtained after trimming the system in such a way to achieve a descent as close as possible to that in [6]. It should be noted that the results of this work were compared and verified with CIMNE's PARASIM6 code for the same simulation conditions.

Figure 3.17 shows the angles and Figure 3.18 the velocity and the aerodynamic coefficients of the system along the descent:

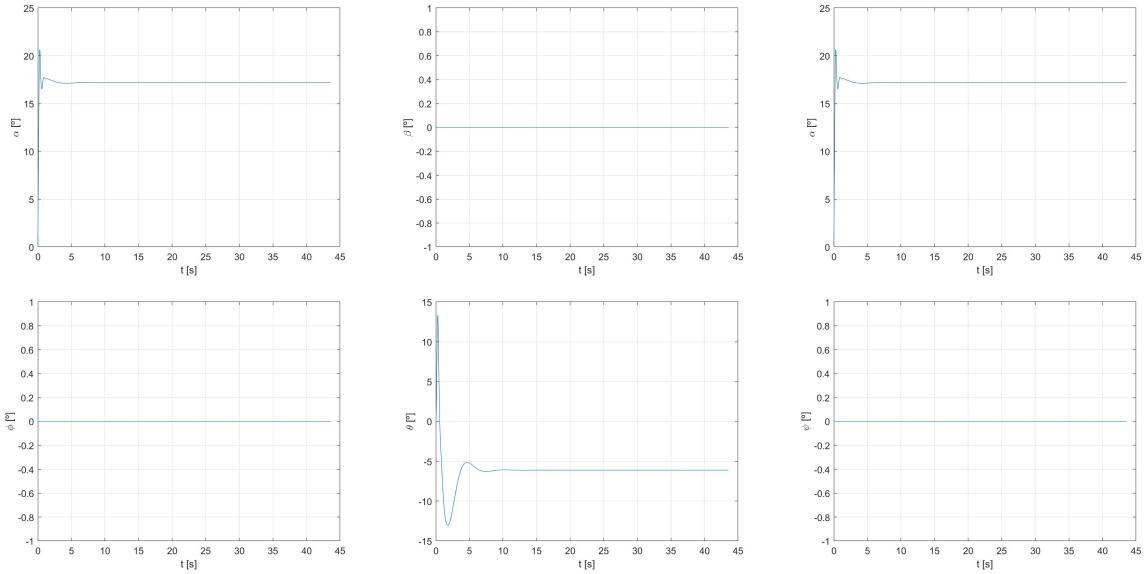

Figure 3.17: Snowflake angles with HVM.

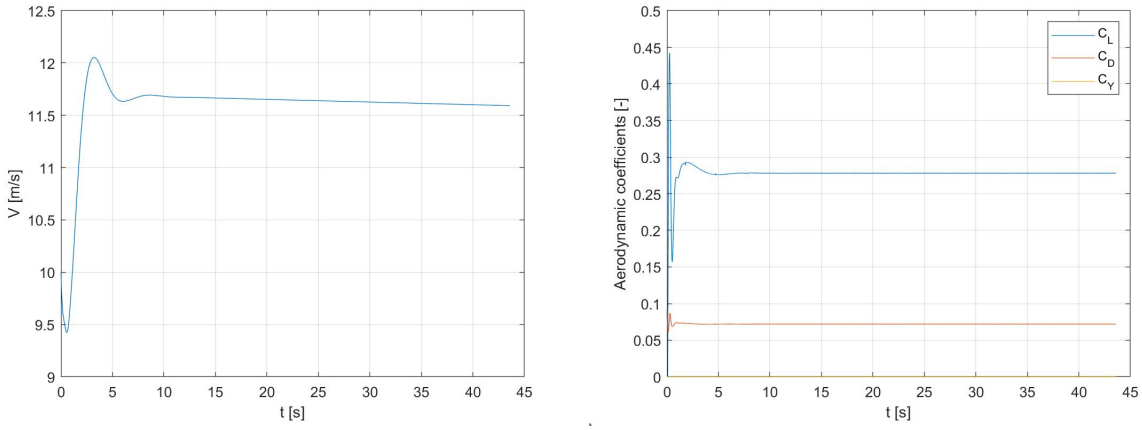

Figure 3.18: Snowflake velocity and aerodynamic coefficients with HVM.

It can be seen how the system stabilizes after a brief transitory state at the beginning of the descent. By not deflecting the flaps, there is no lateral force, so the system only rotates on the y-axis, varying the AoA and pitch. Afterwards, the variation of lift and drag coefficients shows an aerodynamic efficiency of $L/D = 3$, characteristic behavior for parafoils with $AR = 2$ [23].

As mentioned before, according to the Lifting Line Theory considered, the values of the angle of attack must be small because flow separation is not accounted for in a potential approach. This can contrast with the naked eye with the results of the α vs. time graph, but it should not be forgotten that this value is obtained in reference to the body axes of the system and the Snowflake canopy has a rigging angle of -12^o with respect to these axes.

The next step is to adjust the program for the Space Rider conditions and characteristics, trimming the system correctly. In this case, the system is adjusted according to the results of Glouchtchenko in [21], where it is used the same model of parafoil as for the Space Rider. The initial configuration is shown in Table 3.4 and the results from Figure 3.19 to Figure 3.21.

Initial configuration parameters	
Initial linear velocity	[25,0,0] m/s
Initial angular velocity	[0,0,0] rad/s
Initial parafoil attitude	[0,0,0] rad
Initial altitude	200 m
Rigging angle	-7^o
Left/Right CS deflection	0º / 0º
Mass	2550 kg

Table 3.4: Initial configuration parameters with HVM.

These results obtained are very similar to those obtained by Glouchtchenko in [21]. The system reaches $776.17m$ in $35.449s$. As can be seen, the vehicle speed stabilizes and reaches the touchdown at around $22.62m/s$. This speed achieved is an reasonable value. Parafoils with these dimensions and masses usually acquire velocities between 20 and $25m/s$. For example, in [21] it is obtained $23m/s$.

On the other hand, the AoA, path and pitch angles stabilize at acceptable values. Since the pitch stabilizes at 0^o, the system will flight almost parallel to the ground, which is good for a proper landing after the final approach. Furthermore, the aerodynamic coefficients show that the system achieves $C_L/C_D = 4$, expected value for high-performance parafoils with $AR = 3$ such as the Space Rider.

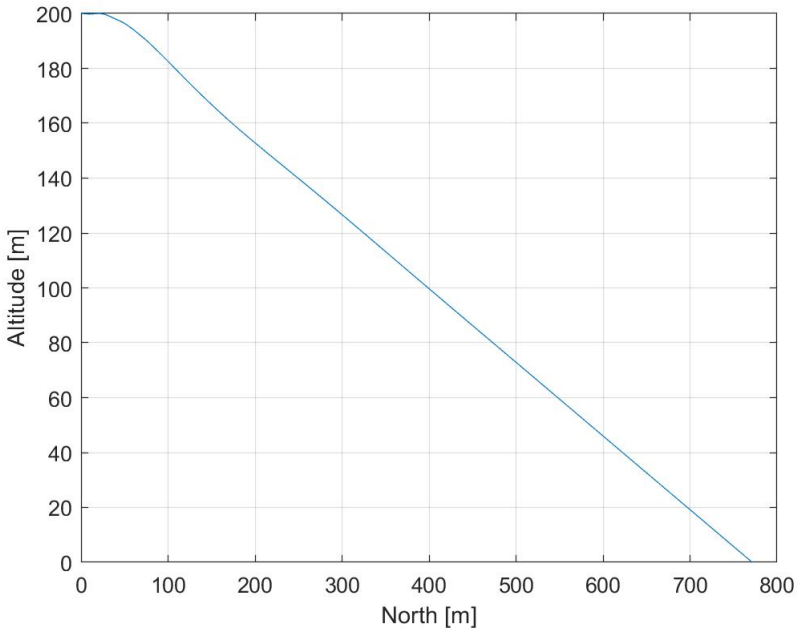

Figure 3.19: Space Rider descent with HVM.

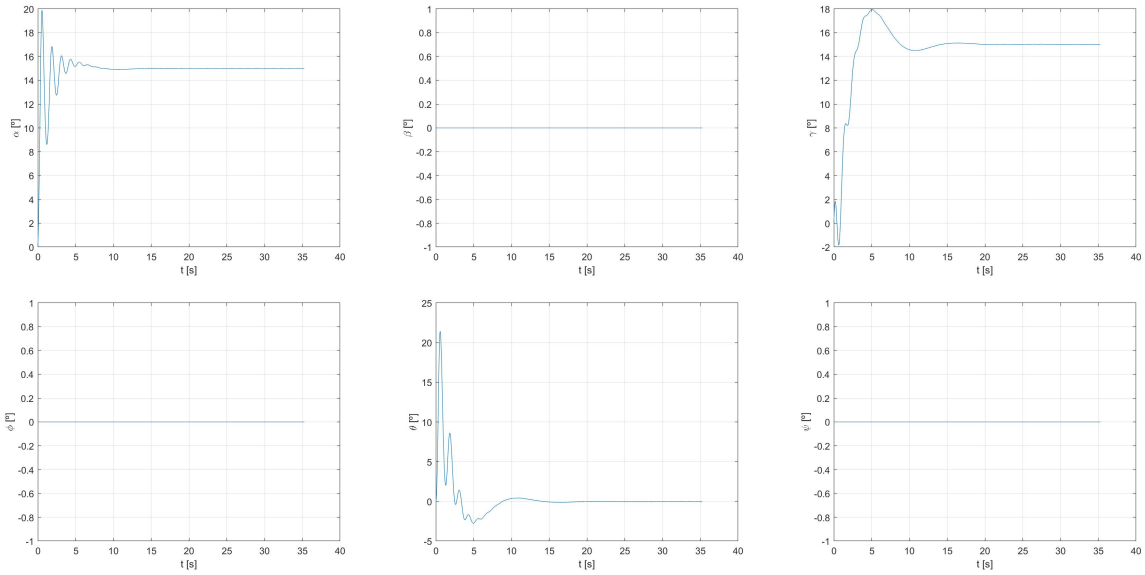

Figure 3.20: Space Rider angles with HVM.

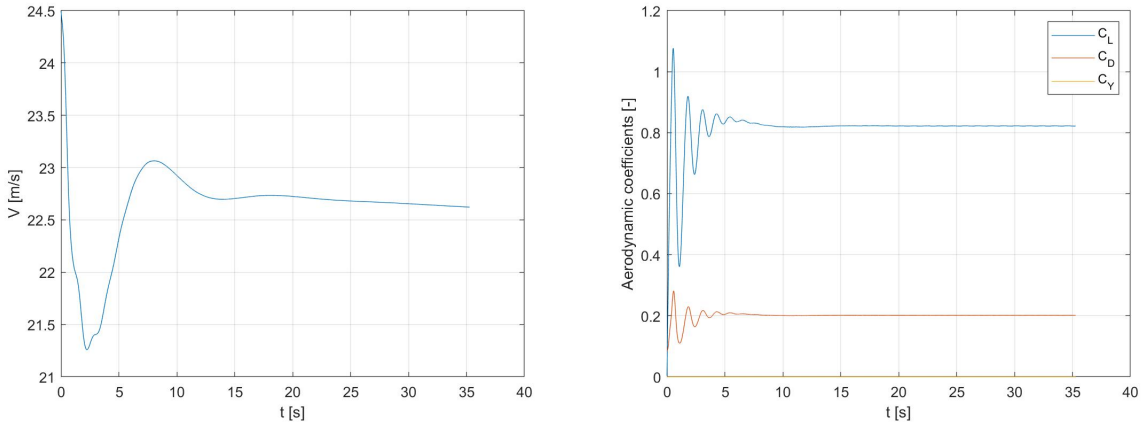

Figure 3.21: Space Rider velocity and aerodynamic coefficients with HVM.

In order to verify the behaviour of the control surfaces deflection and the lateral forces and moments, a descent has been made simulating that proposed in [16]. Between 20 and 50 seconds from release, the right flap is activated. Then, between the 75 and 95 seconds the left one is activated. The rest of the time, both ailerons remain undeflected. The initial configuration is the same as in the previous cases except for the initial height, which starts from $750m$. The results obtained are shown from Figure 3.22 to Figure 3.23. The points in the graphs marked in green indicate the instants in which the ailerons go down, while those marked in red the instants in which they return to their original position.

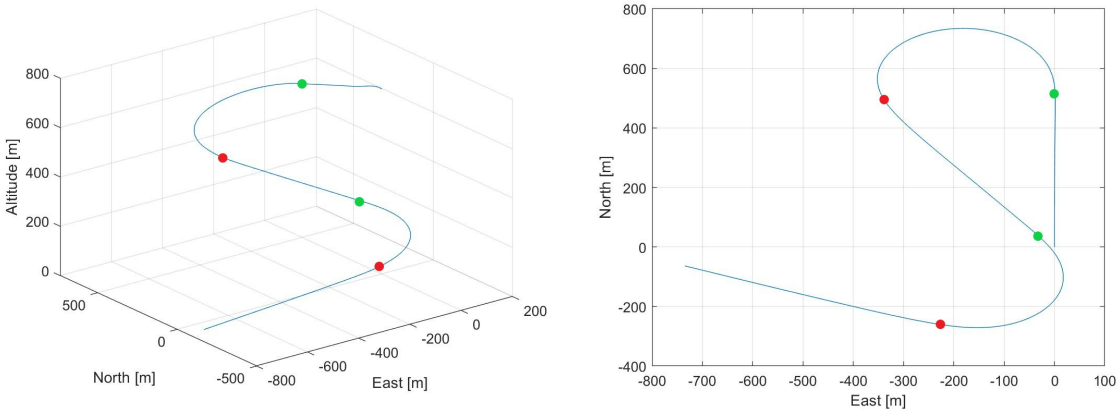

Figure 3.22: Descent with defined trajectory.

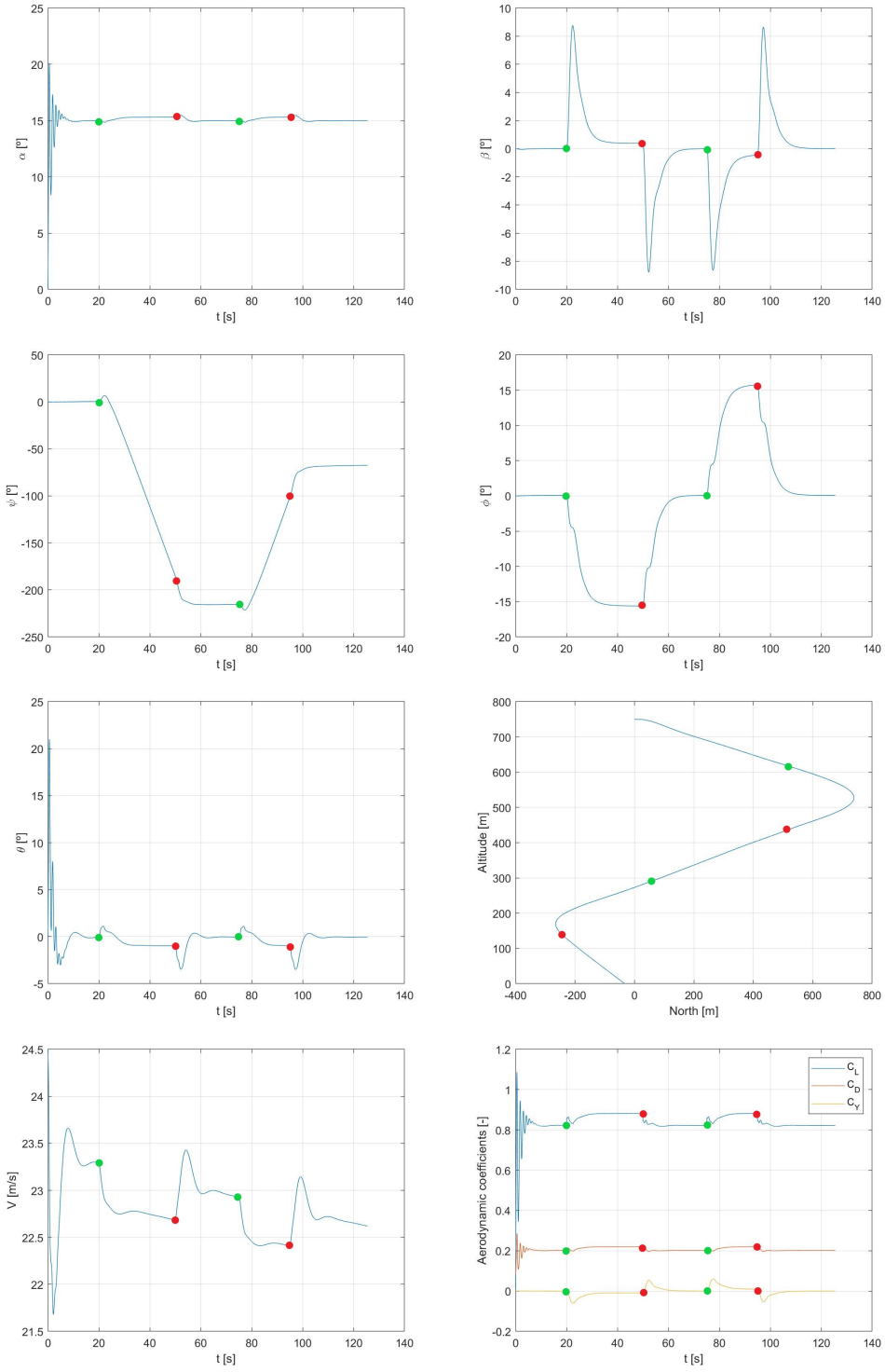

Figure 3.23: Space Rider results for a defined trajectory.

Chapter 4

Guidance, Navigation and Control System

This chapter deals with the Guidance, Control and Navigation (GNC) system. First, the PID methodology is briefly summarized. Then, the GNC system is developed. Finally, the results achieved for the Space Rider are investigated.

4.1 Control System Algorithms

Before describing the operation of the GNC system, the different types of control algorithms are presented. These control algorithms count with 3 types of gain, as the initials of the PID indicate: proportional (P), integral (I) and derivative (D). These control systems can be structured in different ways, as described below [34] [35]:

- P: Proportional controller
  The P algorithm decreases the steady state error of the system. The *Error* is calculated as the difference between the *Desired value* and the *Actual value* by the Eq. 4.1:

$$Error = Desired\ value - Actual\ value \tag{4.1}$$

  This error obtained is then multiplied by the proportional gain (K_p) in order to change the variable controlled by the *Control value*, as shown in Eq. 4.2:

$$Control\ value = K_p \cdot Error \tag{4.2}$$

  With this *Control value* it is possible now to control a parameter, for example the control

surfaces of the parafoil. This controller makes the steady state error decrease while the K_p increases, but it will never get rid of it completely.

- PI: Proportional-Integral controller
  This controller eliminates the steady state error that results from previous P algorithm. It calculates the *Error* as in P controller and the integral gain (K_i) is added multiplying the sum of all previous errors. The *Control value* is calculated as shown in Eq. 4.3:

$$Control\ value = K_p \cdot Error + K_i \cdot SumError \tag{4.3}$$

  Even so, this model is not a good option for the simulator, since its system response is slower than for a P controller. Further, it can not predict the future errors of the system response, just accumulates the previous ones and eliminate oscillations.

- PD: Proportional-Derivative controller
  The PD predicts the future errors, thus increasing the stability of the system. This algorithm includes to the P controller the derivative gain (K_d) multiplied by the difference between the current error and the previous one, as shown in Eq. 4.4:

$$Control\ value = K_p \cdot Error + K_d \cdot \Delta Error \tag{4.4}$$

  As cons, this algorithm is not capable to remove the steady state error as in the PI controller.

- PID: Proportional-Integral-Derivative controller
  It provides the most optimal control dynamics, as it eliminates the steady state error, has a fast system response, good stability and no oscillations. The *Control value* is calculated as a combination of the previous controllers: [35]

$$Control\ value = K_p \cdot Error + K_i \cdot SumError + K_d \cdot \Delta Error \tag{4.5}$$

In this work, the control algorithm that is developed is a PID controller. It can be implemented in two different ways: parallel or serial. Figure 4.1 shows these two structures [34]:

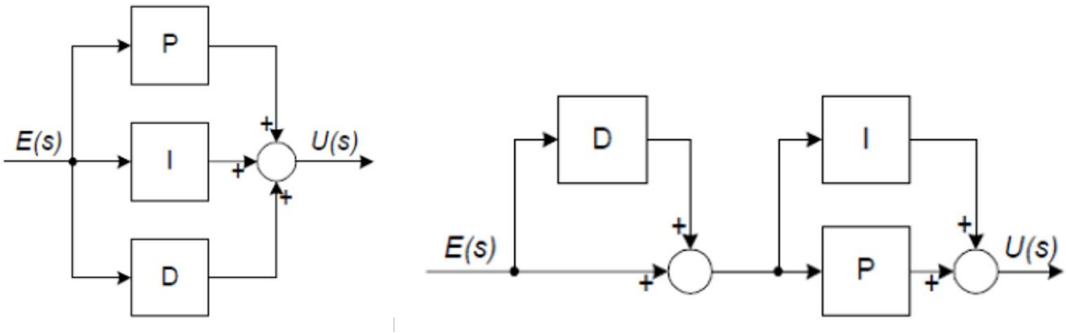

Figure 4.1: Parallel (left) and serial (right) PID systems [22].

For the purpose of the project and due to the linearity of the action parameters on its transfer function ($G(s)$), it has been chosen the parallel PID. Regarding this structure, each action term (P, I, D) is applied directly to the *Error* and can be changed separately without affecting the rest. The transfer function that characterizes this structure is shown below:

$$G(s) = K_p + \frac{K_i}{s} + K_d s \tag{4.6}$$

4.2 GNC

First, the Navigation system estimates the values of the real states of the system required for the Guidance. Once these values are analyzed, the Guidance designs the reference trajectory that the parafoil must follow in order to arrive to the target, or at least the most close possible. Finally, the Control system manages the actuators of the trailing edge ailerons in order to follow the trajectory given by the Guidance.

There are two possible types of control in a lifting body: the longitudinal, which manages the glide slope and therefore the time of the flight; and the lateral-directional control, which attempts to keep the parafoil in the XY-plane. In case of large canopies or wings, as it is assumed for the Space Rider parafoil, both types of control can be decoupled and studied separately in the Guidance and Control systems. The GNC system developed in this work in based on the guidelines proposed in [16] and [22], which study two different strategies for the altitude and lateral control. The lateral one is applied during the whole parafoil descent, checking the parafoil and target position at every time step of the loop, while the altitude one is activated after the parafoil achieves a certain distance from the target.

4.2.1 Navigation System

This system manages the sensor data acquisition and provides the information about the parafoil state (attitude) to the Guidance system. It estimates the position of the system and its velocity in the 3D space by using a GPS unit and an Inertial Unit (IMU), respectively. Despite in the reality there will be some white Gaussian noise that will affect the estimations of these instruments on-board, as it is studied in [21], these fact will not be taken into account. The values of the position and velocity in the GPSim will be taken, as it have been mentioned in Section 2, through the dynamic equations on each step of the loop analyzed during the descent.

4.2.2 Guidance System

This system analyzes the real states of the system provided by the Navigation system and compares them with the landing target, in order to generate the reference trajectory that the parafoil must follow. As mentioned, it estimates separately the variations required in the longitudinal and lateral-directional control actuators in order to perform the correct descent.

- **Longitudinal Guidance**

Also called as altitude guidance, it follows a given Flight Path Attack (FpA) profile, based on tuning to have a direct landing approach or maximizing the time of flight. This FpA is computed at each time step of the loop, providing the value of the glide slope (GS) and then the path angle required in order to perform the landing in the target point.

This strategy is divided in two phases: an initial straight down gliding phase followed by a spiral descent phase, which begins after the deployment and lasts until the target distance is reduced to a defined percentage; and the final one that aims the parafoil to acquire the correct glide slope in order to achieve the target point. The first consists only in lateral guidance and control and the second one combines both control types. In Figure 4.2 it is shown the second phase methodology:

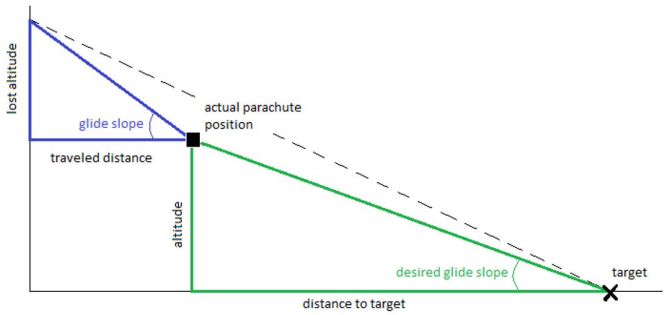

Figure 4.2: Longitudinal control [22].

where the desired glide slope ($GS_{desired}$) is the correct GS required to arrive to the target point, and the glide slope (GS) is the one measured in the current time step. By a simple trigonometrical relation:

$$GS_{real} = \frac{lost\ altitude}{-traveled\ distance} \tag{4.7}$$

$$GS_{desired} = \frac{altitude}{distance\ to\ target} \tag{4.8}$$

The negative sign in Eq. 4.7 is required because the sign of the lost altitude is always negative and the GS must be positive.

- **Lateral-Directional Guidance**

In order to compute the correct trajectory to guide the parafoil in the XY-plane, the literature finds two different ways: inserting a direct 3D trajectory to be followed, for example a T-based model as in [21]; or letting the system compute its own trajectory just giving the landing target, by using a PID as in [22]. The first is interesting in order to allow or establish different considerations during the descent, for example giving the possibility to have multiple possible landing points as backup alternatives or avoid flying above some area as populated ones. However, this project will be focused in the second one because it is desired to use a PID that commands autonomously the perafoil, just introducing the initial and final target point. Furthermore, as it has been used for the longitudinal guidance, the PID structure is very similar in that case and there are successful references as [16] and [22] that demonstrates its good performance.

The methodology used in the lateral guidance is the one developed in [36], which consists on guiding the parafoil from the deployment to the target point by using a yaw-rate command. In Figure 4.3 it is shown the main parameters and functioning of this strategy:

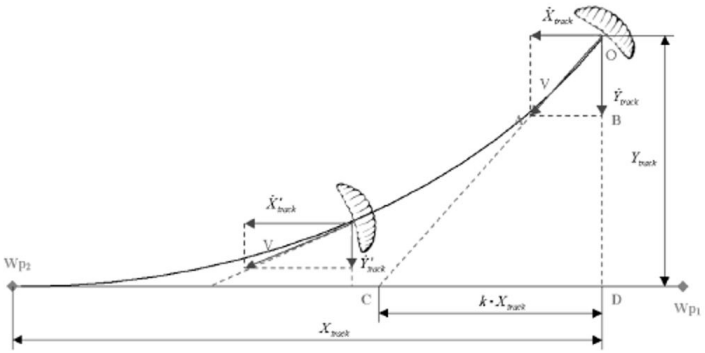

Figure 4.3: Lateral control [16].

where X_{track} and Y_{track} define the parafoil track position measured from Wp_2, V_{ground} is the parafoil ground velocity and C is the interception point. The value of C is obtained considering that the distance on the track line from this point to Wp_2 remains always equal to $(1-k)X_{track}$, at any instant time of the descent, being k a design parameter. By considering the similar geometry of the triangles OAB and OCD, the parafoil position and velocity along time can be obtained in the track frame as shows Eq. 4.9:

$$\frac{\dot{X}_{track}}{K \cdot X_{track}} = \frac{\dot{Y}_{track}}{Y_{track}} \tag{4.9}$$

4.2.3 Control System

This system tracks the trajectory using the information provided by the Guidance system, using a PID, sending orders to the actuators attached to the control surfaces so that the system performs the desired path.

- **Longitudinal Control**

According to Figure 4.2 and the Eq. 4.7 and 4.8, the error con be calculated as:

$$Error = GS_{desired} - GS_{real} \tag{4.10}$$

As it was mentioned in the previous section, the PID used for this cause is based on a parallel structure, which considers the error accumulation ($SumError$) and its difference ($\Delta Error$) on every step analyzed of the loop, as it is shown in the following expressions:

$$SumError[i] = SumError[i-1] + Error[i] \tag{4.11}$$

$$\Delta Error[i] = Error[i-1] - Error[i] \tag{4.12}$$

where $[i]$ means the current instant time and $[i-1]$ the previous one. Applying the characteristic gains of a PID, it is obtained the following equation for the determination of the GS command:

$$GS_{command} = K_p \cdot Error + K_i \cdot SumError + K_d \cdot \Delta Error \tag{4.13}$$

where K_p, K_i and K_d are the proportional, integral and derivative parameters of the PID.

When the system reaches a certain altitude and distance from the target point, the front suspended lines of the parachute pull to modify the Rigging Angle of the system. This action is carried out in order to modify the angles and forces acting on the parafoil so as to descend as close as possible to the landing point. This variation of the Rigging Angle value is controlled according to the following expression:

$$\Gamma = \Gamma_0 + k \cdot GS_{command} \tag{4.14}$$

being Γ the characteristic Rigging Angle of the parafoil (-7^o) and k a defined incidence gain.

- **Lateral-Directional Control**

According to Figure 4.3 and Eq. 4.9, the $Error$ can be calculated as:

$$Error = K \cdot X_{track}\dot{Y}_{track} - Y_{track}\dot{X}_{track} \tag{4.15}$$

In case Eq. 4.15 is not equal to zero, it means that there is a heading error and the magnitude and sign defines the parafoil brake commands. The sign reveals the break that must be activated, while the magnitude or modulus defines the deflection value. The PID used for this case is nearly the same as the used for the longitudinal:

$$SumError[i] = SumError[i-1] + Error[i] \tag{4.16}$$

$$\Delta Error[i] = Error[i-1] - Error[i] \tag{4.17}$$

$$\psi_{command} = K_p \cdot Error + K_i \cdot SumError + K_d \cdot \Delta Error \tag{4.18}$$

Then, the desired yaw-rate is defined by the following equation:

$$\Psi_{desired} = K_R \psi_{command} \tag{4.19}$$

being K_R a design parameter. The yaw-rate is limited to value between $\pm 0.2 rad/s$.

The actuators of the control surfaces of the parafoil are actuated by comparision of this $\Psi_{desired}$ with the actual yaw-rate (Ψ) of the system. This is given by the following equation:

$$\delta = K_{brake}(\Psi_{desired} - \Psi) \tag{4.20}$$

where K_{brake} is a constant which is considered from the kinematics of the parafoil. Regarding this expression, when the difference between both rates is equal to zero, the actuators do not pull the suspended lines and the control surfaces remain undeflected. However, when this does not happen, a break input is generated. The sign obtained for δ defines the semi-span on which the control surface is deflected.

4.3 Final Results

The parameters introduced in the PID for the Space Rider are shown in Table 4.1. The selection of these values has been determined iteratively, from making numerous descents and trying to adjust the most precise results.

PID Parameters	
Kp Glide Slope Command	$-2.2 \cdot 10^{-3}$
Ki Glide Slope Command	$1 \cdot 10^{-5}$
Kd Glide Slope Command	$-1.5 \cdot 10^{-3}$
Kp Yaw Rate Command	$-1.5 \cdot 10^{-5}$
Ki Yaw Rate Command	0.0
Kd Yaw Rate Command	$-1 \cdot 10^{-4}$
K Parameter	0.85
Brake Gain	1
Incidence Angle Gain	1

Table 4.1: PID control parameters for the Space Rider.

As an example of the performance of this system, the parafoil is deployed according to the initial conditions shown in Table 4.2. Figure 4.4 shows the descent trajectory and Figure 4.5 the aerodynamic coefficients and velocity during the descent.

Initial configuration parameters	
Initial linear velocity	[25,0,0] m/s
Initial angular velocity	[0,0,0] rad/s
Initial parafoil attitude	[0,0,0] rad
Initial altitude	2000m
Rigging angle	-7^o
Mass	2550 kg
Target Position North	1100m
Target Position East	-1900m

Table 4.2: Initial configuration parameters with PID.

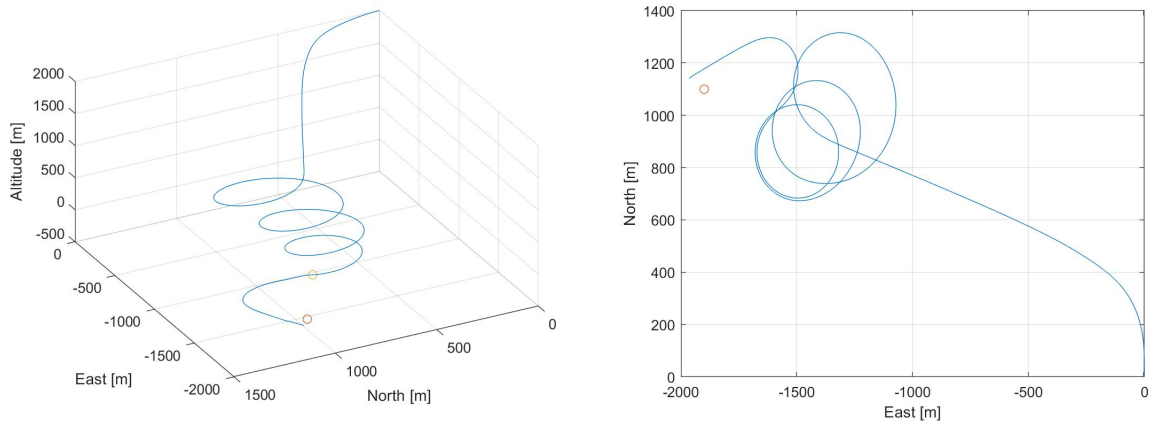

Figure 4.4: Space Rider descent with GNC.

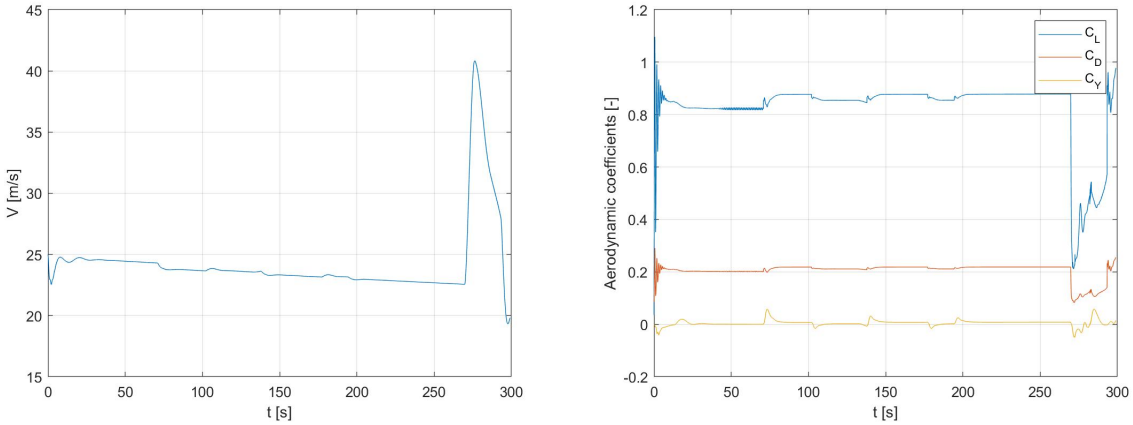

Figure 4.5: Space Rider descent velocity and aerodynamic coefficients with GNC.

The descent shows the three stages in which the GNC operates: target orientation, loiter and final approach. When the system reaches the last $10m$ of altitude, the "flare" maneuver is activated. In this phase the ailerons are deflected up to an angle of 50^o in order to increase the aerodynamic forces and reduce considerably the total speed of the system. The landing takes place at $76.76m$ far from the destination with an horizontal and vertical speed of speed of $22.3m/s$ and $3.2m/s$, respectively. These results meet the mission requirements for this last phase of the Space Rider re-entry.

Finally, Figure 4.6 also shows the three stages of the descent and the "flare" maneuver by the results of the angles of the system:

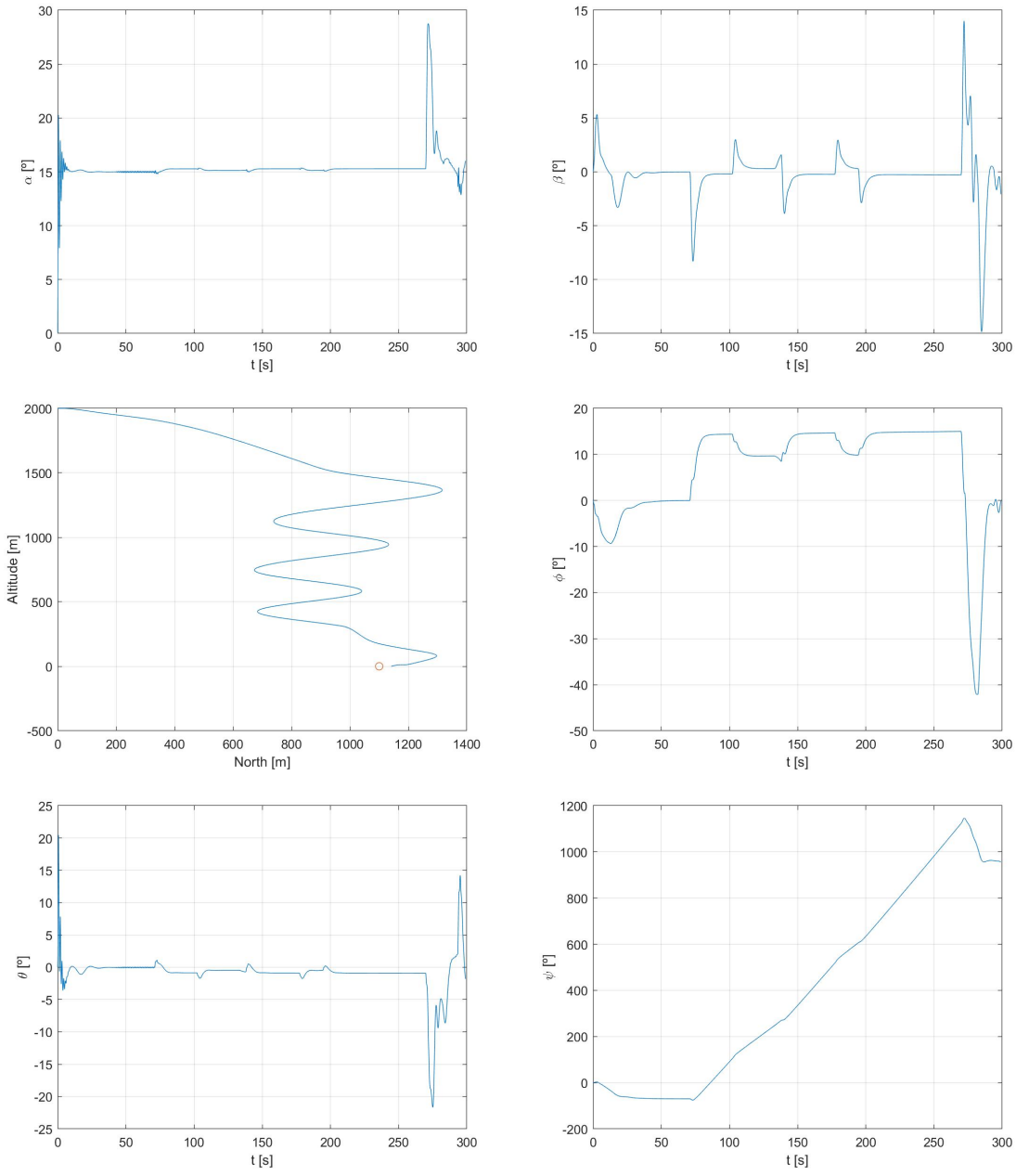

Figure 4.6: Space Rider descent results with GNC.

Conclusions

The main objective of this work was to develop a program capable of simulating guided descent and landing of atmospheric re-entry space vehicles. For this work, the parafoil-payload system of the future ESA's Space Rider mission has been taken as a study model. This work has become a challenge, since this autonomous guided parafoil phase application is truly innovative in this sector and that there are not many accessible references of similar descents since the re-entry of the NASA's X-38 vehicle in 2002. However, after developing the dynamic solver and time integrator, applying the HVM and introducing the GNC system, it can be concluded that satisfactory results have been obtained.

In the development of this work, the GPSim program developed in [6] and later by [22] was firstly analyzed and improved. This was tedious work, which meant understanding the structure of the entire program with all its numerous subroutines, searching for and correcting possible bugs and taking into account new considerations in order to optimize its performance. The GPSim program was based on the parameters and conditions of the small Snowflake system, so, after introducing the HVM and validating the correct operation of the program, it was adapted to the parafoil-payload system of the Space Rider. After adjusting the parameters of the new system into the program, the results obtained show a satisfactory behavior, verifying the correct behavior of the simulator.

Regarding the use of the HVM in the aerodynamic code, the simulation time has been reduced compared to the VLM methodology used before, since the iterative numerical program does not have to perform so many calculations at each time step of the descent. For a $2000m$ height descent, the HVM takes 15 minutes CPU-time, while the VLM takes more than an hour. Moreover, the comparisons with other works show that accurate results can be obtained with the HVM, closer to those obtained by other more complex and computationally expensive methods. In this way, it has been possible to significantly reduce the simulation time, obtaining approxi-

mations with acceptable errors according to the main objective of the work.

On the other hand, it has been possible to demonstrate that the GNC system developed based on a PID control algorithm is applicable and adapts well to the requirements of this work. This allows to steer autonomously, and in a simple way, the Space Rider vehicle to a very small distance from the landing target point, controlling the descent and landing speed satisfactorily. In addition, it can be expected that by optimizing the values of the design parameters of the PID, even more accurate trajectories could be obtained.

Although the developed GPSim simulator has primarily an academic purpose, that is, for its use in the educational field, it can also be used to obtain good parachute descent approaches for more complex studies. Simulations for complex projects such as the Space Rider mission, are designed and proved with very sophisticated and precise programs. Normally, these simulations are obtained by using powerful supercomputers and HPC systems, which currently have high computational costs that require long implementation time and consume large quantities of energy. In this way, the GPSim allows to obtain quite acceptable estimations, to experiment with the main variables of the descent in a fast and effective way. This can reduce the number of simulated descents with more powerful programs, thus reducing significantly the computational costs.

Future Work

First of all, although several validations of the operation of the simulator have already been carried out throughout the work, it would be advisable to try to find more validations that justify the correct operation of the program.

In this work, the behavior of the system during the gliding parachute deployment has not been studied, nor the previous ribbon parachute deployed before. It would be interesting to study these phases of the descent, perform a transitory analysis of the system and link all the results obtained. Also, the study has been simplified to a 6 DoF simulator with the mere objective of reducing the complexity of the program. Regarding this last aspect, the number of DoFs could be increased to study the system, separating the parafoil from the Space Rider vehicle, then analyzing their behavior separately and how they interact. In this way, the tensions in the connecting lines that join both systems could also be computed, thus knowing the stresses with which both bodies have to deal with along the descent.

Regarding the autonomous parafoil system, the CNG system could be improved finding the most optimal PID parameters for the descent or using other more precise methodologies, such as the use of the T-based strategy proposed in [21]. In addition, a PID could also be developed that directly controls the control surfaces from the conventional longitudinal and lateral-directional control parameters, using the fundamental flight mechanics control equations and the coefficients obtained in other works or references. Also, the PID could be designed with Simulink, showing a more characteristic interface or tool for an automatic control problem.

On the other hand, Matlab shows the results graphically and provides good numerical results necessary for the evaluation of this program. However, it would also be interesting to be able to link the Matlab simulation with all its variables to another 3D simulation program, with a CAD design of the parafoil, that visually and attractively simulates the descent.

Another aspect to consider is program optimization, trying to make it more efficient, improving the management of calculations and variable calls, detailing better tolerances and time steps in the loop and using computational efficiency techniques. In this way, the program can be developed with another more efficient programming language than Matlab, such as C ++, Python or Fortran. Using a more efficient program can significantly reduce computing costs, thus achieving faster simulations.

Finally, the methodology used to develop the GPSim simulator could be applicable to other parachute models and even other types of aircraft, such as drones or flying wings. The program could be modified slightly by introducing the new desired parameters, as well as adding new control surfaces that help stabilize and control the trajectory during the descent.

Environmental Impact

The environmental impact of this work could only be based on the electric energy consumption required for its development and the environmental repercussions that the production of this energy entails. Fortunately, these amounts are so insignificant that they can be neglected.

On the other hand, the development of this project can be seen as an energy saving for the future and bring benefits. As it has been proved, the GPSim allows to obtain quite acceptable estimations of the descent, to vary and check the main variables of the system in a fast and effective way. This fact can reduce considerably the number of simulated descents with more powerful programs and computers, thus reducing the electric energy consumption and the emissions that this consumption implies.

References

[1] COCKRELL, D. and YOUNG, A., *The aerodynamics of parachutes*. North Atlantic Treaty Organization, Advisory Group for Aerospace Research Development. Neuilly-sur-Seine: AGARD, no. 295, 1987. ISBN: 92-835-0422-4.

[2] KERMAN, B., "A Brief History of the Parachute." [Online]. Popular Mechanics, 29 February 2012. [Accessed: 15 December 2019]. Available from: `https://www.popularmechanics.com/flight/g815/a-brief-history-of-the-parachute/`.

[3] BROOKFIELD, K. and COOPER, D., "Leonardo da Vinci - Parachute." [Online]. The British Library, 5 January 2004. [Accessed: 20 December 2019]. Available from: `https://www.bl.uk/onlinegallery/features/leonardo/parachute.html`.

[4] VERANZIO, F., "Homo Volans." [Online]. Library of Congress. [Accessed: 20 December 2019]. Available from: `https://www.loc.gov/item/2006690488/`.

[5] TIKKANEN, A., "André-Jacques Garnerin." [Online]. Encyclopaedia Britannica, 27 January 2020. [Accessed: 20 December 2019]. Available from: `https://www.britannica.com/biography/Andre-Jacques-Garnerin`.

[6] PÉREZ, D. and ORTEGA, E., "Study of a methodology for the flight simulation of ram-air parachutes using a vortex-lattice aerodynamic model". Degree's thesis, UPC, Escola Superior d'Enginyeries Industrial, Aeroespacial i Audiovisual de Terrassa, 10 June 2017.

[7] GUTTMAN, J., "Heinecke Parachute: A Leap of Faith for WWI German Airmen." [Online]. HistoryNet. [Accessed: 20 December 2019]. Available from: `https://www.historynet.com/heinecke-parachute-a-leap-of-faith-for-wwi-german-airmen.htm`.

[8] LEE, G., "BAE Systems DA4 landing." [Online]. Eurofighter Typhoon. [Accessed: 20 January 2020]. Available from: `https://www.eurofighter.com/multimedia/details/bae-systems-da4-landing-with-brake-chute-at-warton-england-the-607`.

[9] PALLARDY, R., "Parachutes." [Online]. Encyclopaedia Britannica, 20 March 2019. [Accessed: 10 January 2020]. Available from: `https://www.britannica.com/technology/parachute`.

[10] JALBERG, D., "Rogallo's Target Kite." [Online]. Kite Patents. [Accessed: 23 December 2019]. Available from: `https://kitepatents.wordpress.com/2006/04/10/jalberts-parafoil-us3285546/`.

[11] PETTY, J., "X-38: Crew Return Vehicle." [Online]. NASA, 4 February 2000. [Accessed: 23 December 2019]. Available from: `https://spaceflight.nasa.gov/history/station/x38/parafoil.html`.

[12] BENNETT, T. and FOX, R., "Design, development & flight testing of the NASA X-38 7,500 ft2 parafoil recovery system," in *17th AIAA Aerodynamic Decelerator Systems Technology Conference and Seminar*. American Institute of Aeronautics and Astronautics, Monterey, California, May 2003. DOI: 10.2514/6.2003-2107.

[13] NASA, "X-38 Landing." [Online]. NASA, 2000. [Accessed: 23 December 2019]. Available from: `https://es.wikipedia.org/wiki/Archivo:X-38_Landing_(cropped).jpg`.

[14] DUNKER, S., "Ram-air wing design considerations for airborne wind energy," in *Green Energy and Technology*. Springer, Berlin, Heidelberg, 2 October 2013. pp. 517–546. ISSN: 1865-3529, DOI: 10.1007/978-3-642-39965-7_31.

[15] BERLAND, J. *et al.*, "Development of a low cost 10,000 lb capacity ram-air parachute, DRAGONFLY program," in *18th AIAA Aerodynamic Decelerator Systems Technology Conference and Seminar*. American Institute of Aeronautics and Astronautics, Munich, May 2005. pp. 258–272. DOI: 10.2514/6.2005-1626.

[16] GONZÁLEZ, E. *et al.*, "Development of a 6-DoF simulator for analysis and evaluation of autonomous parafoil systems." Publication CIMNE Nº-356, April 2011.

[17] HUART, J., "Space Rider." [Online]. ESA, 1 June 2017. [Accessed: 10 November 2019]. Available from: `https://spaceflight.nasa.gov/history/station/x38/parafoil.html`.

[18] MARINI, M. *et al.*, "Aeroshape Trade-Off and Aerodynamic Analysis of the Space-Rider Vehicle," in *7th EUCASS European Conference for Aeronautics and Space Sciences*. Politecnico di Milano, Milan, July 2017. DOI: 10.13009/EUCASS2017-416.

[19] ESA, "Space Rider: Europe's reusable space transport system." [Online]. ESA, 5 June 2019. [Accessed: 10 November 2019]. Available from: `https://www.esa.int/Enabling_Support/Space_Transportation/Space_Rider_Europe_s_reusable_space_transport_system`.

[20] BALOSSINO, A. *et al.*, "Conceptual Design of the Descent Subsystem for the Safe Atmospheric Re-Entry Flight of Space Rider," in *7th EUCASS European Conference for Aeronautics and Space Sciences*. Politecnico di Milano, Milan, July 2017. DOI: 10.13009/EUCASS2017-624.

[21] GLOUCHTCHENKO, N., "Multibody parafoil-payload model for SpaceRider trajectory". Master's thesis, Politecnico di Milano, 4 July 2018.

[22] GUTIÉRREZ, D. and ORTEGA, E., "Study and implementation of a control system for autonomous guided parachutes". Degree's thesis, UPC, Escola Superior d'Enginyeries Industrial, Aeroespacial i Audiovisual de Terrassa, 10 June 2018.

[23] LINGARD, J., "Ram-air parachute design," in *13th AIAA Aerodynamic Decelerator Systems Technology Conference and Seminar*. American Institute of Aeronautics and Astronautics, Clearwater Beach, Florida, May 1995. pp. 1–51.

[24] LISSAMAN, P. and BROWN, G., "Apparent mass effects on parafoil dynamics," in *AIAA/AHS/ASEE Aerospace Design Conference*. American Institute of Aeronautics and Astronautics, Irvine, February 1993. pp. 445–451. DOI: 10.2514/6.1993-1236.

[25] KOWALECZKO, G., "Apparent mass and inertia moments of the parafoil." *Journal of Theoretical and Applied Mechanics*, vol. 52, no. 3, pp. 606–616, January 2014. ISSN: 1429-2955.

[26] YAKIMENKO, O., *Precision Aerial Delivery Systems: Modeling, Dynamics, and Control*. Reston, Virginia: American Institute of Aeronautics and Astronautics, 2015. DOI: 10.2514/4.101960, ISBN: 978-1-62410-195-3.

[27] TWEDDLE, B., "Simulation and Control of Guided Ram Air Parafoils." Tech. Report. University of Waterloo, Department of Electrical and Computer Engineering, 29 August 2006. Available from: `https://waterloouav.files.wordpress.com/2010/01/parachute.pdf`.

[28] SLEGERS, N. and COSTELLO, M., "Aspects of Control for a Parafoil and Payload System." *Journal of Guidance, Control, and Dynamics*, vol. 26, pp. 898–905, May 2003.

[29] GÓMEZ, M.A.; PÉRES, M. and PUENTES, C., *Mecánica del vuelo*. Madrid: Garceta, 2 ed., 2012. ISBN: 978-84-1545-201-0.

[30] YOTOV, N. and KALUSHKOV, I., "Paraglider Structure, Materials and Maintenance." [Online]. SkyNomad, 2020. [Accessed: 3 March 2020]. Available from: `http://skynomad.com/articles/paraglider_construction.html`.

[31] FRANCHINI, S. and LÓPEZ, O., *Introducción a la Ingeniería Aeroespacial*. Garceta, 2 ed., 2012. ISBN: 978-84-9281-290-5.

[32] BARROWS, T., "Apparent mass of parafoils with spanwise camber." *Journal of Aircraft*, vol. 39, no. 3, pp. 445–451, May 2002. DOI: 10.2514/2.2949.

[33] ORTEGA, E., "Horseshoe Vortex Method." UPC, Escola Superior d'Enginyeries Industrial, Aeroespacial i Audiovisual de Terrassa, 2018.

[34] NEJJARI, F. and QUEVEDO, J., "Disseny de reguladors." UPC, Escola Superior d'Enginyeries Industrial, Aeroespacial i Audiovisual de Terrassa, 2018.

[35] TEMEL, S.; YALI, S. and GOREN, S., "P, pd, pi, pid controllers." Tech. Report. Middle East Technical University, Electrical and Electronics Engineering Department, 2013. Available from: `https://www.academia.edu/27666692/EE402RecitationReport`.

[36] NICULESCU, M., "Lateral track control law for Aerosonde UAV," in *39th Aerospace Sciences Meeting and Exhibit*. American Institute of Aeronautics and Astronautics, Reno, Nevada, January 2001. DOI: 10.2514/6.2001-16.